Monthly Notices of the ROYAL ASTRONOMICAL SOCIETY

MNRAS **502,** 3704–3722 (2021) doi:10.1093/mnras/staa3960
Advance Access publication 2020 December 28

TOI-257b (HD 19916b): a warm sub-saturn orbiting an evolved F-type star

Brett C. Addison [1]★ Duncan J. Wright,[1]★ Belinda A. Nicholson,[2,1] Bryson Cale,[3] Teo Mocnik,[4] Daniel Huber,[5] Peter Plavchan [3] Robert A. Wittenmyer,[1]★ Andrew Vanderburg,[6] William J. Chaplin,[7,8] Ashley Chontos [5,9] Jake T. Clark [1] Jason D. Eastman [10] Carl Ziegler [11] Rafael Brahm,[12,13] Bradley D. Carter,[1] Mathieu Clerte,[1] Néstor Espinoza [14] Jonathan Horner,[1] John Bentley,[32] Andrés Jordán,[16,13] Stephen R. Kane,[4] John F. Kielkopf,[17] Emilie Laychock,[18] Matthew W. Mengel [1] Jack Okumura,[1] Keivan G. Stassun [19,20] Timothy R. Bedding [21,8] Brendan P. Bowler,[22] Andrius Burnelis,[30] Sergi Blanco-Cuaresma [10] Michaela Collins,[18] Ian Crossfield,[23,24] Allen B. Davis,[25] Dag Evensberget [1] Alexis Heitzmann,[1] Steve B. Howell [27] Nicholas Law,[28] Andrew W. Mann,[28] Stephen C. Marsden,[1] Rachel A. Matson [26] James H. O'Connor,[1] Avi Shporer,[31] Catherine Stevens,[30] C. G. Tinney,[32] Christopher Tylor,[1] Songhu Wang,[15] Hui Zhang,[33] Thomas Henning,[34] Diana Kossakowski,[34] George Ricker,[31,62] Paula Sarkis,[34] Martin Schlecker,[34] Pascal Torres,[29] Roland Vanderspek,[31] David W. Latham,[10] Sara Seager,[31,35] Joshua N. Winn,[36] Jon M. Jenkins,[37] Ismael Mireles,[31] Pam Rowden [38] Joshua Pepper [39] Tansu Daylan,[31] Joshua E. Schlieder,[40] Karen A. Collins,[10] Kevin I. Collins [3] Thiam-Guan Tan [41] Warrick H. Ball [7,8] Sarbani Basu,[25] Derek L. Buzasi,[43] Tiago L. Campante [44,45] Enrico Corsaro,[46] L. González-Cuesta [47,48] Guy R. Davies,[7,8] Leandro de Almeida [49] Jose-Dias do Nascimento, Jr [49,10] Rafael A. García,[50,51] Zhao Guo,[52] Rasmus Handberg [8] Saskia Hekker [60,61,8] Daniel R. Hey,[21,8] Thomas Kallinger,[54] Steven D. Kawaler,[55] Cenk Kayhan [56] James S. Kuszlewicz [53,8] Mikkel N. Lund [8] Alexander Lyttle,[7,8] Savita Mathur,[47,48] Andrea Miglio [7,8] Benoit Mosser,[57] Martin B. Nielsen,[7,8,42] Aldo M. Serenelli [58,59] Victor Silva Aguirre[8] and Nathalie Themeßl[53,8]

Affiliations are listed at the end of the paper

Accepted 2020 December 10. Received 2020 December 9; in original form 2020 January 20

ABSTRACT

We report the discovery of a warm sub-Saturn, TOI-257b (HD 19916b), based on data from NASA's Transiting Exoplanet Survey Satellite (*TESS*). The transit signal was detected by *TESS* and confirmed to be of planetary origin based on radial velocity observations. An analysis of the *TESS* photometry, the MINERVA-Australis, FEROS, and HARPS radial velocities, and the asteroseismic data of the stellar oscillations reveals that TOI-257b has a mass of $M_P = 0.138 \pm 0.023$ M$_J$ (43.9 ± 7.3 $M_\oplus$), a radius of $R_P = 0.639 \pm 0.013$ R$_J$ (7.16 ± 0.15 R$_\oplus$), bulk density of $0.65^{+0.12}_{-0.11}$ (cgs), and period $18.38818^{+0.00085}_{-0.00084}$ days. TOI-257b orbits a bright (V = 7.612 mag) somewhat evolved late F-type star with $M_* = 1.390 \pm 0.046$ M$_{sun}$, $R_* = 1.888 \pm 0.033$ R$_{sun}$, $T_{\rm eff} = 6075 \pm 90$ K, and $v \sin i = 11.3 \pm 0.5$ km s^{-1}. Additionally, we find hints for a second non-transiting sub-Saturn mass planet on a ∼71 day orbit using the radial velocity data. This system joins the ranks of a small number of exoplanet host stars (∼100) that have been characterized with asteroseismology. Warm sub-Saturns are rare in the known sample of exoplanets, and thus the discovery of TOI-257b is important in the context of future work studying the formation and migration history of similar planetary systems.

Key words: asteroseismology – techniques: photometric – techniques: radial velocities – techniques: spectroscopic – planetary systems – stars: individual (TIC 200723869/TOI-257).

1 INTRODUCTION

When Mayor & Queloz (1995) announced the discovery of the first hot Jupiter, 51 Pegasi b, astronomers were baffled by the existence of a Jovian planet orbiting its host star with such a short orbital period (about 4.2 days). That discovery revolutionized our understanding

★ E-mail: Brett.Addison@usq.edu.au (BCA); Duncan.Wright@usq.edu.au (DJW); Rob.Wittenmyer@usq.edu.au (RAW)

of the planet formation process, revealing the situation to be more complex than had been expected based on studies of the Solar System (e.g. Lissauer 1993). Radial velocity and transit surveys over the past two decades have uncovered numerous warm and hot giant exoplanets with orbital periods shorter than 100 days (see, e.g. Butler et al. 1997; Bayliss et al. 2013; Brahm et al. 2016; Van Eylen et al. 2018; Dawson et al. 2019; Kipping et al. 2019), and occurrence studies based on those discoveries suggest that such planets can be found orbiting ∼ 1 per cent of all Sun-like stars (e.g. Howard et al. 2010, 2012; Santerne et al. 2012; Wright et al. 2012; Santerne et al. 2016; Zhou et al. 2019) (in comparison to an occurrence rate of at least 7 per cent for more distant planets; see, e.g. Foreman-Mackey et al. 2016; Wittenmyer et al. 2020).

In addition to the Solar System lacking a hot Jupiter, it also lacks other broad classes of planets such as super-Earths and mini-Neptunes ($\sim$1.5−3 $R_\oplus$) as well as planets larger than Neptune and smaller than Saturn, known as sub-Saturns (which we have defined as planets with a radius between ∼5 and 8 $R_\oplus$). Sub-Saturns are a key class of planets to study for understanding the formation, migration, and compositions of giant planets in general. Their large size requires a significant H/He envelope that comprises a majority of their planetary volume, yet their masses are sufficiently small that their cores are not degenerate (unlike for planets near the mass of Jupiter). This means that modelling the interiors of sub-Saturns can be simplified as a planet consisting of a high-density core surrounded by extended H/He envelope and where measurements of mass and radius enable a single family of solutions for the planet's core and envelope mass fraction (e.g. Weiss & Marcy 2014; Petigura et al. 2016; Pepper et al. 2017; Petigura et al. 2017).

It is commonly thought that close-in giant planets, such as hot/warm Jupiters and sub-Saturns, do not form *in situ*, but instead originate beyond the protostellar ice line (typically located at several astronomical units from the host star) where there is sufficient solid material available to build up ∼5−20 $M_\oplus$ cores (Pollack et al. 1996; Weidenschilling 2005; Rafikov 2006). In the case of Jovian planets, once their cores reach this critical mass regime, they begin to rapidly accrete gas from the protoplanetary disk to form their gaseous envelopes. This process continues until the disk is dispersed (Rafikov 2006; Tanigawa & Ikoma 2007), resulting in Jupiter-sized planets with masses of ∼100−10 000 $M_\oplus$. For sub-Saturns, however, the runaway accretion of gas appears to either not have occurred at all or did occur but in a gas-depleted disk (Lee, Chiang & Ferguson 2018). As a result, sub-Saturns have masses that range from ∼10 to 100 $M_\oplus$. The mass of a sub-Saturn is strongly correlated with the metallicity of its host star, but is uncorrelated with the resulting radial size (Petigura et al. 2017).

The sample of measurements for longer period ($P \geq 10$ d) 'warm' giants and sub-Saturns thus far is small. The detection of more of these systems is then important to better constrain the formation and migration mechanisms of close-in planets.

One such source of warm giant planetary systems is NASA's *Transiting Exoplanet Survey Satellite* (*TESS*, Ricker et al. 2015), launched on 2018 April 18. As of 2019 November 6, the *TESS* mission has delivered a total of 1361 planetary candidates – objects that require further observations from ground-based facilities to confirm the existence of the candidate exoplanets.[1] To date, such follow-up observations have resulted in a total of 34 confirmed planetary discoveries (e.g. Nielsen et al. 2019; Quinn et al. 2019; Vanderburg et al. 2019; Wang et al. 2019) – and it is likely that many more planets will be confirmed in the months to come.

During its initial 2-year primary mission, *TESS* is expected to discover several dozen warm Jupiters, Saturns, and sub-Saturns orbiting bright ($V < 10$ mag) stars (Sullivan et al. 2015; Barclay, Pepper & Quintana 2018; Huang et al. 2018). Those planets will be suitable targets for follow-up observations to measure their masses, through radial velocity measurements, to probe their atmospheric compositions, through transmission and emission spectroscopy, and to determine their spin-orbit angles through measurements of the Rossiter-McLaughlin effect.

In this work, we report the discovery of one such planet, TOI-257b (HD 19916b), based on photometric data obtained by *TESS*, and follow-up observations using the MINERVA-Australis facility at the University of Southern Queensland's Mt. Kent Observatory (Wittenmyer et al. 2018; Addison et al. 2019), the FEROS instrument ($R =$ 48 000, Kaufer et al. 1999) on the MPG 2.2 m telescope at La Silla Observatory, and the HARPS spectrograph ($R = 120\,000$, Mayor et al. 2003) on the ESO 3.6 m telescope at La Silla Observatory. The details of the spectrographs and spectroscopic observations are provided in Section 2.3.

In Section 2, we describe the *TESS* photometric data, and the reduction of the MINERVA-Australis spectroscopic data and the radial velocity pipeline, as well as radial velocities collected with other instruments. Section 3 presents the analysis of the data, including the characterization of the host star, the derived properties of the planet, and the limits on any additional planets in the system. In Section 4, we compare TOI-257b with the demographics of the known exoplanets, and discuss the significance of the system. We provide concluding remarks and suggestions for future work in Section 5.

2 OBSERVATIONS AND DATA REDUCTION

TOI-257 (HD 19916) is a bright (V = 7.612 mag) late F-type star, located at a distance of 77.1 ± 0.2 pc (parallax of 12.9746 ± 0.0327 mas from *Gaia* DR2, Gaia Collaboration 2018a). The star is slightly evolved with a radius of 1.888 ± 0.033 $R_\odot$, mass of 1.390 ± 0.046 $M_\odot$, and surface gravity of $\log g = 4.030 \pm 0.011$ dex, derived from the asteroseismic analysis of the *TESS* photometry in Section 3.2. The star has an effective temperature of 6075 ± 90 K and metallicity of [M/H] = 0.19 ± 0.10 derived from the analysis of MINERVA-Australis spectra in Section 3.1 as well as a rotational velocity of $v \sin i = 11.3 \pm 0.5$ km s^{-1} in Section 3.3. TOI-257 has rotational period of 8.07 ± 0.27 days based on analysis of the *TESS* photometry in Section 3.3.

2.1 *TESS* photometry

The star TOI-257 (HD 19916, TIC 200723869 Stassun et al. 2019) was observed in Sectors 3 and 4 by Camera 3 of the *TESS* spacecraft in 2-min cadence mode nearly continuously between 2018 September 22 and 2018 November 15. The photometric data were processed by the Science Processing Operations Center (SPOC) pipeline as described in Jenkins et al. (2016). Overall, three transits were detected with depth of ∼1500 parts per million (ppm) and duration of ∼6 h. Two transits are detected in Sector 3 (on BJD 2458386 and BJD 2458404), and one in Sector 4 (on BJD 2458422). The transit at the beginning of Sector 3 was observed during an experiment to

[1] Data from the NASA Exoplanet Archive, 2019 November 6.

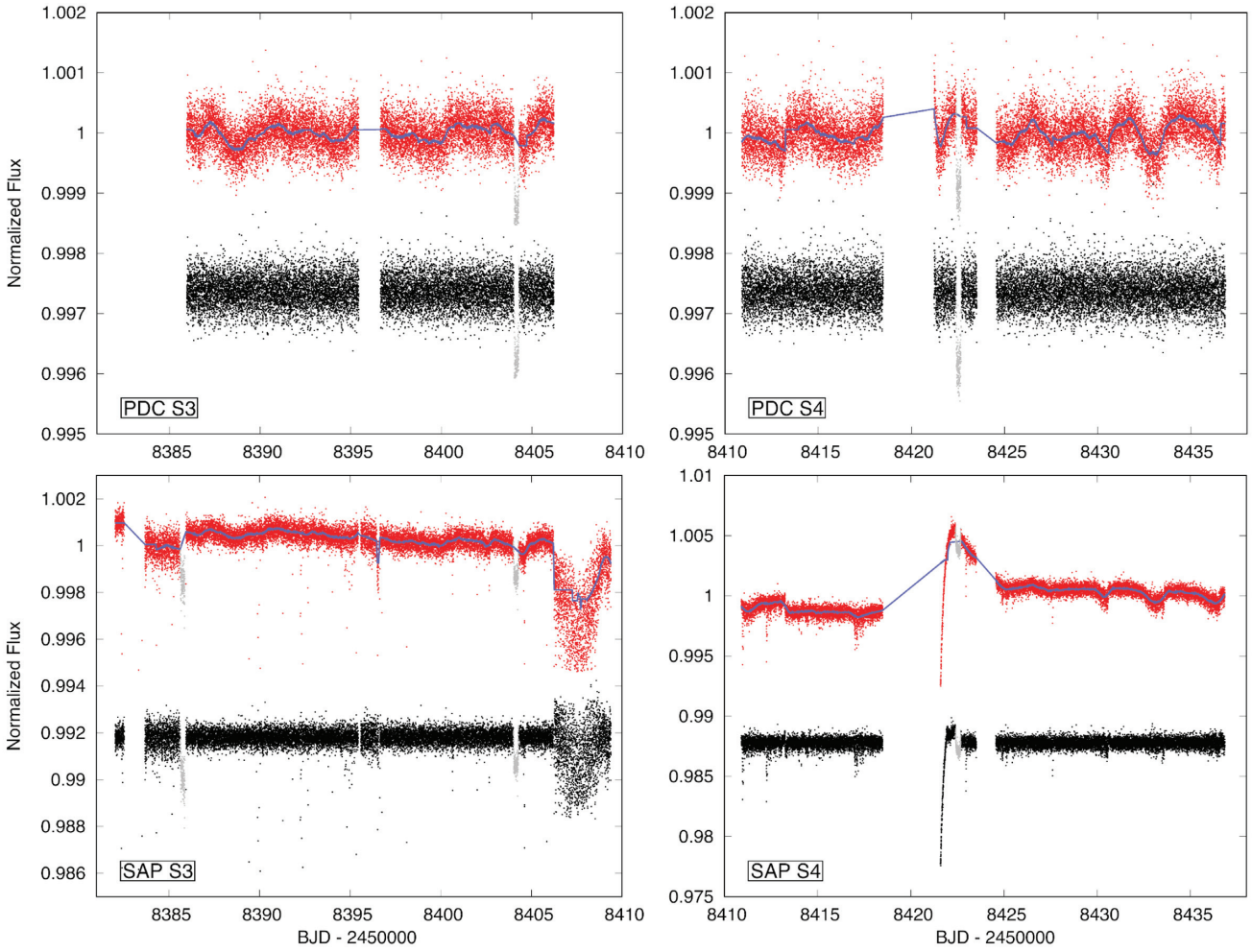

Figure 1. *TESS* light curves of TOI-257 from Sector 3 (left panel) and Sector 4 (right panel). The pre-search data conditioning (PDC, upper panels) and simple aperture photometry (SAP, lower panels) versions of the light curves before (shown in red) and after detrending (shown in black and shifted down arbitrarily to avoid overlap with the red points). The detrending function is blue and transits are grey. Top left: A single transit event was recovered by PDC in Sector 3. Top right: A single transit event was recovered by PDC in Sector 4. Bottom left: Two transit events were recovered by SAP from Sector 3. Bottom right: A single transit event was recovered by SAP in Sector 4.

improve the spacecraft pointing,[2] and the transit in Sector 4 was observed during the thermal ramp.

The *TESS* light curves were accessed from the NASA's Mikulski Archive for Space Telescopes. The light curves had been processed by the *TESS* team using two different techniques: pre-search data conditioning (PDC, the usual way of light curve extraction and removal of systematics, see, Jenkins et al. 2016) and simple aperture photometry (SAP, see, Twicken et al. 2010). These raw SAP and PDC light curves are shown in Fig. 1, along with their detrended versions.

To detrend the PDC light curves, we removed all quality-flagged data (except for stray light flag 2048), clipped 5σ outliers, removed stellar and instrumental variability, normalized with the mean of the out-of-transit flux, and merged together Sectors 3 and 4. To remove the photometric variability, we used a Savitzky-Golay (SG) filter with a kernel width of 501 data points and a polynomial of order 2 over 3 iterations. During detrending, the planetary transits were masked and then detrended by dividing out the interpolated SG-filtered flux values from the out-of-transit data points. The SG detrending removed any longer-period stellar variability and systematics, and retained any features that occurred on timescales comparable or shorter than the duration of planetary transits (Kinemuchi et al. 2012; Jenkins et al. 2016).

Two transits were recovered using the PDC technique, one in Sector 3 and one in Sector 4. The transit at the beginning of Sector 3 was missed by the PDC procedure since it falls on the part of the light curve that was quality-flagged for manual exclusion during a spacecraft pointing improvement experiment. To recover the first transit in Sector 3, we performed the exact same detrending procedure on the SAP version of the light curve as on the PDC light curve, the only difference being that the manual exclusion (flag 128) data points were not removed. The resulting detrended SAP light curve was used for recovering the first transit observed by *TESS* in Sector 3 but this version of the light curve was not used in the global fit analysis as systematics were not removable as seen in Fig. 1. Indeed the noise level is higher (by ∼200 ppm) in the detrended SAP light curve just prior to this transit event.

[2]See the data release notes at https://archive.stsci.edu/missions/tess/doc/tess_drn/tess_sector_03_drn04_v02.pdf

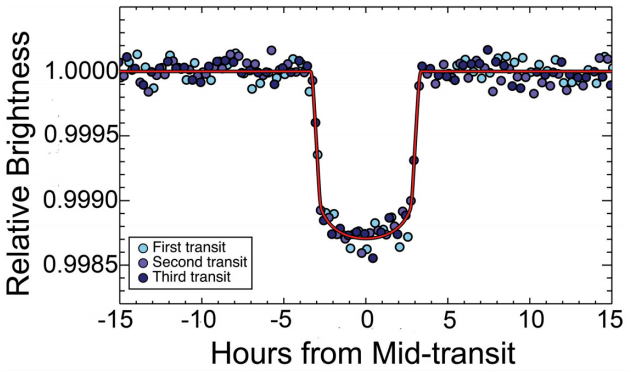

Figure 2. Phase folded *TESS* light curve of TOI-257 binned at a cadence of 30 min with the individual transits colour coded showing that they are of similar depth. The first transit comes from the custom light curve where we removed systematics that are the result of a spacecraft pointing anomaly. The second and third transit are from the pre-search data conditioning light curve. The red curve is the best-fitting transit model.

To include the first transit from Sector 3 in the global fit analysis, we created a custom light curve following the procedures of Vanderburg et al. (2019) to obtain a cleaner light curve relatively free from systematics and stellar variability. We started by using a larger 4.5 pixel radius aperture to extract the Sector 3 photometry, which reduced the amplitude of the systematics observed in the early part of the light curve compared to the *TESS* pipeline's SAP light curve. We then removed systematics from a small segment of the light curve surrounding the first transit (BJD 2458383.7 $< t <$ 2458388.0) by decorrelating against the median background flux value from outside the aperture for each 2-min image and the standard deviation of the Q1, Q2, and Q3 quaternions within each 2-min exposure. We excluded points during the planet transit in our decorrelation to prevent the systematics correction from biasing or distorting the shape of the transit. Next, we simultaneously fit the low-frequency variability (which we modeled as a basis spline) with a transit model in a similar manner to Vanderburg et al. (2016a), except that we did not also simultaneously fit for the systematics and we introduced a discontinuity at BJD 2458385.95 where we switch from the custom light curve to the PDC light curve. The combination of our custom light curve and the PDC light curve are what we use in the final global fitting analysis with EXOFASTv2 (Eastman, Gaudi & Agol 2013; Eastman 2017; Eastman et al. 2019). Fig. 2 is the resulting 30-min binned and phase folded custom light curve along with the PDC light curve and the individual transits colour coded.

2.2 Direct imaging follow-up

If a target star has a close companion, the additional flux from the second source can cause photometric contamination, resulting in an underestimated planetary radius, or be the source of an astrophysical false positive. To rule out the presence of close companions, speckle imaging observations were taken of TOI-257 with the SOAR and Zorro instruments.

2.2.1 SOAR speckle imaging

TOI-257 was observed with SOAR speckle imaging (Tokovinin 2018) on 2019 February 18 UT, observing in a similar visible bandpass as *TESS*. The 5σ detection sensitivity and the speckle auto-correlation function from the SOAR observation are plotted in Fig. 3. Further details of the observations are available in Ziegler et al. (2020). No nearby stars were detected within 3″ of TOI-257.

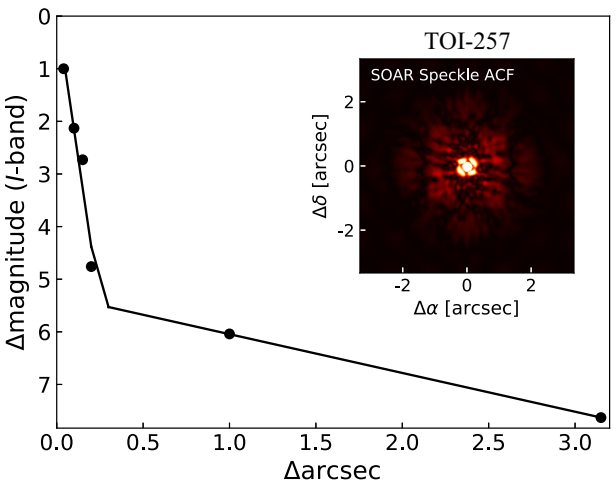

Figure 3. The 5σ detection sensitivity and inset speckle auto-correlation function from SOAR speckle observing of TOI-257 on 2019 February 18 UT in *I*-band, which is similar to the *TESS* bandpass. The orientation of the inset image has North pointed up and East to the left. No stars were detected within 3″ of TOI-257.

2.2.2 Gemini-South high-resolution speckle imaging using Zorro

Direct imaging observations of TOI-257 was also carried out on 2019 September 12 UT using the Zorro speckle instrument on Gemini-South.[3] Zorro simultaneously provides speckle imaging in two bands, 562 and 832 nm, with output data products including a reconstructed image, and robust limits on companion detections (Howell et al. 2011). Fig. 4 shows our 562 nm result and reconstructed speckle image and we find that TOI-257 is indeed a single star with no companion brighter than about 6 magnitudes detected within 1.75″. This limit corresponds to approximately an M3V star at the inner working angle of ∼0.25″ and M5V at the outer working angle of ∼1.75″.

2.3 Spectroscopy

We obtained high-resolution spectroscopic observations of TOI-257 with MINERVA-Australis, FEROS, and HARPS to confirm and measure the mass of the *TESS* transiting planet candidate. Here we describe the observations from each spectrograph and list the derived radial velocities in Table 2.

2.3.1 High-resolution spectroscopy with MINERVA-Australis

The MINERVA-Australis facility is an array of five independently operated 0.7 m CDK700 telescopes located at the Mount Kent Observatory in Queensland, Australia (see, Addison et al. 2019, for a detailed description of the facility). Designed as a robotic observatory, instruments are remotely accessible and can be operated both in manual or automatic configurations. Four of the telescopes in the array (T2, T3, T4, T6) simultaneously feed stellar light to a single KiwiSpec R4-100 high-resolution spectrograph via fiber optic

[3]https://www.gemini.edu/sciops/instruments/alopeke-zorro/

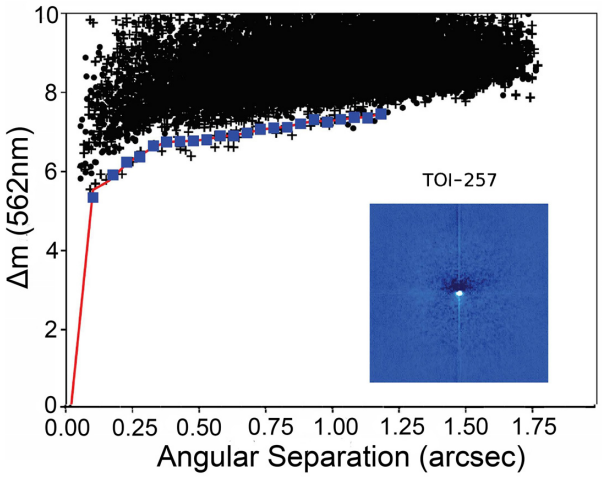

Figure 4. Zorro speckle observation of TOI-257 taken at 562 nm. Our simultaneous 832 nm observation provides a similar result. The red line fit and blue points represent the 5σ fit to the sky level (black points) revealing that no companion star is detected from the diffraction limit (17 mas) out to 1.75″ within a Δ mag of 6 to 8. The inset reconstructed speckle image has north up and East to the left and is 2.5″ across.

cables. Only three out of the four telescopes, T3, T4, and T6, were used for spectroscopic observations of TOI-257.

A total of 53 spectra (observations taken simultaneously from multiple telescopes in the array are counted as one observation) of TOI-257 were obtained at 28 epochs between 2019 July 12 and October 15. Each of the telescopes in the MINERVA-Australis array simultaneously feed via 50 μm circular fiber cables a single KiwiSpec R4-100 high-resolution ($R = 80\,000$) spectrograph (Barnes et al. 2012) with wavelength coverage from 480 to 630 nm.

Radial velocities are derived for each telescope using the least-squares technique of Anglada-Escudé & Butler (2012) and corrected for spectrograph drifts with simultaneous Thorium-Argon (ThAr) arc lamp observations. We observed TOI-257 with up to three telescopes simultaneously with one or two 20 to 30-minute exposures per epoch, resulting in a signal-to-noise ratio between 30 and 80 per resolution element at ∼550 nm.

The radial velocities from each telescope are given in Table 2 labeled by their fiber number. Each telescope (fiber) has its own velocity zero-point which is modeled as a free parameter, and the mean internal uncertainty estimate of the MINERVA-Australis observations is 4.6 m s^{-1}. The radial velocities collected by MINERVA-Australis show a ∼10 m s^{-1} sinusoidal variation (RMS uncertainty of 13.9 m s^{-1} based on the residuals from the EXOFASTv2 one-planet fit) that is in phase with the photometric ephemeris with an amplitude compatible with a sub-Saturn-sized planet on a circular orbit as shown in Figs 9 and 10. Additionally, we measured the bisector velocity span (BVS) values using the cross-correlation functions as a check to ensure that the radial velocity variation observed is not from stellar activity or a background eclipsing binary system. As shown in Fig. 11, no correlations are apparent in the BVS values.

2.3.2 *High-resolution spectroscopy with the fiber-fed extended range optical spectrograph*

TOI-257 was observed with the fiber-fed extended range optical spectrograph (FEROS) instrument ($R = 48\,000$, Kaufer et al. 1999) on the MPG 2.2 m telescope at La Silla Observatory between 2018 December 15 and 2019 January 22. We collected a total of eight spectra and the observations were performed in simultaneous calibration mode, utilizing the ThAr arc lamp on the secondary fiber to track and remove instrumental variations due to changes in the temperature and pressure during the science exposures. The exposure times were set to 300 s, resulting in signal-to-noise ratio between 270 and 370 per resolution element at ∼510 nm. We produced radial velocities by cross-correlation with a G2-type binary mask template using the CERES pipeline (Brahm, Jordán & Espinoza 2017a), which also corrects the radial velocities for instrumental systematics and the Earth's motion.

Table 1. Stellar parameters for TOI-257.

Parameter	Value	Source
R.A. (hh:mm:ss)	03:10:03.982	*Gaia* DR2
Decl. (dd:mm:ss)	-50:49:56.58	*Gaia* DR2
μ_α (mas yr^{-1})	97.912 ± 0.052	*Gaia* DR2
μ_δ (mas yr^{-1})	27.911 ± 0.082	*Gaia* DR2
Parallax (mas)	12.9746 ± 0.0327	*Gaia* DR2
A_V (mag)	0.0165 (≤ 0.0506) †, ⋆	Schegel dust maps
Broadband magnitudes:		
B_T (mag)	$8.293^{+0.020}_{-0.016}$ ‡	Tycho
V_T (mag)	$7.612^{+0.020}_{-0.011}$ ‡	Tycho
TESS (mag)	7.012 ± 0.017	*TESS* TIC v6
J (mag)	6.504 ± 0.020 ‡	2MASS
H (mag)	6.325 ± 0.020 ‡	2MASS
K_s (mag)	6.256 ± 0.020 ‡	2MASS
*WISE*1 (mag)	6.209 ± 0.100 ‡	WISE
*WISE*2 (mag)	6.084 ± 0.033 ‡	WISE
*WISE*3 (mag)	$6.239^{+0.030}_{-0.015}$ ‡	WISE
*WISE*4 (mag)	$6.172^{+0.100}_{-0.048}$ ‡	WISE
Gaia (mag)	$7.417^{+0.020}_{-0.000}$ ‡	*Gaia* DR2
$Gaia_{BP}$ (mag)	$7.730^{+0.020}_{-0.002}$ ‡	*Gaia* DR2
$Gaia_{RP}$ (mag)	$6.994^{+0.020}_{-0.002}$ ‡	*Gaia* DR2
Spectroscopic properties from MINERVA-Australis spectra (preferred solution):		
$T_{\rm eff}$ (K)	6075 ± 90 †	iSpec; this paper
log *g* (dex)	3.97 ± 0.10	iSpec; this paper
[M/H] (dex)	0.19 ± 0.10 †	iSpec; this paper
$R_\star$ ($R_\odot$)	1.926 ± 0.017	isochrones; this paper
$M_\star$ ($M_\odot$)	$1.389^{+0.056}_{-0.009}$	isochrones; this paper
$\rho_\star$ (g cm^{-3})	0.275 ± 0.011	isochrones; this paper
$L_\star$ ($L_\odot$)	4.527 ± 0.120	isochrones; this paper
Age (Gyr)	3.11 ± 0.46	isochrones; this paper
$v \sin i$ (km s^{-1})	11.3 ± 0.5	LSD; this paper
Spectroscopic properties from HARPS spectra:		
$T_{\rm eff}$ (K)	6178 ± 80	ZASPE; this paper
log *g* (dex)	4.06 ± 0.11	ZASPE; this paper
[Fe/H] (dex)	0.32 ± 0.05	ZASPE; this paper
$v \sin i$ (km s^{-1})	10.2 ± 0.5	ZASPE; this paper

Notes.–†Priors used in the EXOFASTv2 global fit.
‡Broadband magnitudes used in the EXOFASTv2 Spectral Energy Distribution analysis.
⋆Upper limit on the V-band extinction from Schegel dust maps.

Table 2. Journal of radial velocity observations of TOI-257.

Date (BJD)	RV ($m\,s^{-1}$)	σ ($m\,s^{-1}$)	Instrument
2458465.539980	21.9	2.0	HARPS
2458465.602650	26.7	2.0	HARPS
2458465.690670	26.1	2.0	HARPS
2458466.529660	24.8	2.0	HARPS
2458466.591590	17.1	2.0	HARPS
2458466.678080	23.5	2.0	HARPS
2458466.682320	22.5	2.0	HARPS
2458467.674470	12.5	5.3	FEROS
2458468.663190	8.1	5.5	FEROS
2458481.588670	20.9	2.0	HARPS
2458481.593290	24.6	2.0	HARPS
2458481.597630	24.1	2.0	HARPS
2458482.673800	32.1	2.0	HARPS
2458482.678140	29.7	2.0	HARPS
2458493.714430	− 11.4	6.2	FEROS
2458497.608960	− 10.3	5.7	FEROS
2458500.629830	− 19.3	5.7	FEROS
2458505.566740	− 14.6	5.9	FEROS
2458677.272975	10.8	3.0	M-A Tel3
2458677.272975	− 13.2	3.4	M-A Tel4
2458677.294387	24.3	3.1	M-A Tel3
2458677.294387	10.3	3.4	M-A Tel4
2458680.203692	11.6	3.6	M-A Tel3
2458680.203692	20.7	4.1	M-A Tel4
2458680.203692	− 8.2	7.5	M-A Tel6
2458680.225093	0.1	3.9	M-A Tel3
2458680.225093	3.3	3.8	M-A Tel4
2458680.225093	5.4	8.0	M-A Tel6
2458681.170185	1.9	3.5	M-A Tel3
2458681.170185	22.1	3.6	M-A Tel4
2458681.170185	− 8.3	4.6	M-A Tel6
2458681.191597	− 3.8	3.3	M-A Tel3
2458681.191597	− 11.9	3.9	M-A Tel4
2458681.191597	14.9	4.6	M-A Tel6
2458682.146655	25.4	3.9	M-A Tel3
2458682.146655	27.6	7.2	M-A Tel4
2458682.146655	12.7	5.3	M-A Tel6
2458682.168067	14.9	3.9	M-A Tel3
2458682.168067	19.6	4.6	M-A Tel4
2458682.168067	5.0	5.6	M-A Tel6
2458683.249780	6.3	3.5	M-A Tel4
2458683.276111	− 5.9	4.6	M-A Tel3
2458683.276111	14.6	3.3	M-A Tel4
2458688.201840	5.1	3.0	M-A Tel3
2458688.201840	− 0.1	3.3	M-A Tel4
2458688.201840	− 22.9	6.0	M-A Tel6
2458688.223252	− 23.0	2.8	M-A Tel3
2458688.223252	− 5.6	3.1	M-A Tel4
2458688.223252	− 25.9	6.5	M-A Tel6
2458689.179745	− 2.6	3.5	M-A Tel3
2458689.179745	1.9	4.1	M-A Tel4
2458689.179745	4.6	5.1	M-A Tel6
2458689.201146	0.1	3.1	M-A Tel3
2458689.201146	− 0.9	3.5	M-A Tel4
2458689.201146	13.6	4.4	M-A Tel6
2458694.193565	17.4	2.6	M-A Tel3
2458694.193565	22.3	2.9	M-A Tel4
2458694.193565	28.4	3.8	M-A Tel6
2458694.214965	8.0	2.5	M-A Tel3
2458694.214965	3.3	2.7	M-A Tel4
2458694.214965	9.7	3.8	M-A Tel6
2458695.195069	7.9	2.8	M-A Tel3
2458695.195069	16.6	3.2	M-A Tel4
2458695.195069	26.1	3.7	M-A Tel6
2458708.118403	20.7	3.6	M-A Tel3
2458708.118403	10.3	4.7	M-A Tel4
2458708.118403	7.4	5.5	M-A Tel6
2458708.139815	15.4	3.3	M-A Tel3
2458708.139815	− 0.5	4.0	M-A Tel4
2458708.139815	4.4	4.9	M-A Tel6
2458710.171273	3.3	3.7	M-A Tel3
2458710.171273	21.9	3.7	M-A Tel4
2458710.171273	− 9.4	4.6	M-A Tel6
2458710.192674	13.6	3.5	M-A Tel3
2458710.192674	14.9	3.4	M-A Tel4
2458710.192674	13.0	4.4	M-A Tel6
2458712.165914	34.1	3.7	M-A Tel3
2458712.165914	12.5	3.9	M-A Tel4
2458712.165914	10.9	4.6	M-A Tel6
2458712.187326	34.5	3.4	M-A Tel3
2458712.187326	12.9	3.7	M-A Tel4
2458712.187326	20.1	4.3	M-A Tel6
2458714.125567	4.3	5.0	M-A Tel3
2458714.125567	− 0.6	5.6	M-A Tel4
2458714.125567	− 7.3	6.4	M-A Tel6
2458714.146979	27.6	4.5	M-A Tel3
2458714.146979	− 9.1	4.8	M-A Tel4
2458714.146979	6.2	5.6	M-A Tel6
2458715.217465	12.2	2.7	M-A Tel3
2458715.217465	15.8	3.8	M-A Tel4
2458715.217465	− 8.1	4.2	M-A Tel6
2458715.238877	6.6	2.6	M-A Tel3
2458715.238877	− 4.4	3.5	M-A Tel4
2458715.238877	6.2	4.1	M-A Tel6
2458716.222002	− 15.2	2.6	M-A Tel3
2458716.222002	7.3	4.0	M-A Tel4
2458716.222002	1.9	4.3	M-A Tel6
2458716.243403	− 15.5	2.6	M-A Tel3
2458716.243403	− 0.9	4.0	M-A Tel4
2458716.243403	− 6.4	4.2	M-A Tel6
2458719.145729	− 36.6	3.4	M-A Tel3
2458719.145729	− 38.1	3.9	M-A Tel4
2458719.145729	− 22.8	4.8	M-A Tel6
2458720.110220	− 17.3	3.1	M-A Tel3
2458720.110220	− 24.6	3.8	M-A Tel4
2458720.110220	− 37.4	4.8	M-A Tel6
2458720.131632	− 29.8	3.0	M-A Tel3
2458720.131632	− 24.1	3.7	M-A Tel4
2458720.131632	− 29.0	4.4	M-A Tel6
2458722.130023	− 5.8	3.3	M-A Tel3
2458722.130023	− 16.4	5.7	M-A Tel4
2458722.130023	− 14.2	4.9	M-A Tel6
2458722.151435	− 16.2	3.2	M-A Tel3
2458722.151435	− 8.9	5.8	M-A Tel4
2458722.151435	− 21.1	4.8	M-A Tel6
2458725.111910	− 8.4	2.9	M-A Tel3
2458725.111910	12.8	5.1	M-A Tel4
2458725.111910	− 20.3	4.6	M-A Tel6
2458725.133322	5.0	2.8	M-A Tel3
2458725.133322	− 25.7	5.1	M-A Tel4
2458725.133322	10.8	4.4	M-A Tel6
2458728.105961	− 2.4	3.1	M-A Tel3
2458728.105961	− 4.3	4.2	M-A Tel4
2458728.105961	15.3	4.3	M-A Tel6
2458728.127373	− 1.2	3.1	M-A Tel3
2458728.127373	22.4	4.0	M-A Tel4
2458728.127373	28.7	4.2	M-A Tel6
2458729.072407	− 1.2	3.9	M-A Tel3

Table 2 – *continued*

Table 2 – *continued*

Date (BJD)	RV ($m\,s^{-1}$)	σ ($m\,s^{-1}$)	Instrument
2458729.072407	– 10.4	4.4	M-A Tel4
2458729.072407	– 6.1	5.4	M-A Tel6
2458729.093808	– 2.2	3.7	M-A Tel3
2458729.093808	8.2	4.4	M-A Tel4
2458729.093808	4.2	5.4	M-A Tel6
2458729.115220	– 15.5	3.6	M-A Tel3
2458729.115220	5.8	4.2	M-A Tel4
2458729.115220	– 2.7	5.3	M-A Tel6
2458730.018252	– 1.8	5.2	M-A Tel3
2458730.018252	– 2.9	7.5	M-A Tel4
2458730.018252	– 2.0	6.7	M-A Tel6
2458730.039664	25.0	4.4	M-A Tel3
2458730.039664	– 4.7	4.7	M-A Tel4
2458730.039664	– 3.9	5.9	M-A Tel6
2458734.108032	21.5	3.7	M-A Tel3
2458734.108032	7.9	4.4	M-A Tel4
2458734.108032	– 17.1	5.2	M-A Tel6
2458734.129444	– 5.7	3.5	M-A Tel3
2458734.129444	0.4	4.1	M-A Tel4
2458734.129444	33.6	4.4	M-A Tel6
2458735.062465	3.5	3.9	M-A Tel3
2458735.062465	– 22.2	4.5	M-A Tel4
2458735.062465	1.7	5.3	M-A Tel6
2458735.083877	– 1.0	3.7	M-A Tel3
2458735.083877	– 22.1	4.4	M-A Tel4
2458735.083877	11.7	5.0	M-A Tel6
2458737.059757	– 17.9	4.1	M-A Tel3
2458737.059757	– 13.1	4.7	M-A Tel4
2458737.059757	– 28.1	4.7	M-A Tel6
2458737.081169	– 13.7	3.9	M-A Tel3
2458737.081169	– 11.8	4.4	M-A Tel4
2458737.081169	– 6.5	4.7	M-A Tel6
2458739.195799	– 23.8	3.5	M-A Tel3
2458739.195799	5.5	5.0	M-A Tel4
2458739.195799	– 15.9	4.4	M-A Tel6
2458739.217211	– 23.8	3.7	M-A Tel3
2458739.217211	– 15.5	4.2	M-A Tel4
2458739.217211	5.5	4.9	M-A Tel6
2458741.221794	– 3.5	3.5	M-A Tel3
2458741.221794	6.5	3.7	M-A Tel4
2458741.221794	4.1	4.6	M-A Tel6
2458742.066331	19.7	5.3	M-A Tel3
2458742.066331	– 17.8	4.3	M-A Tel4
2458742.066331	– 11.7	6.2	M-A Tel6
2458760.781220	32.2	2.3	HARPS
2458762.784910	23.1	2.0	HARPS
2458764.688350	39.6	2.0	HARPS
2458765.692580	38.7	2.5	HARPS
2458772.692230	23.3	2.0	HARPS
2458773.680520	34.7	2.1	HARPS
2458774.741390	24.4	2.0	HARPS
2458775.824000	9.3	2.6	HARPS
2458777.807510	15.8	3.2	HARPS
2458780.869940	21.2	9.7	HARPS
2458802.637920	21.6	2.0	HARPS
2458804.705790	37.1	2.0	HARPS
2458806.677240	26.1	2.0	HARPS
2458810.664000	14.8	2.0	HARPS
2458811.725990	7.1	2.0	HARPS
2458813.686300	20.1	2.0	HARPS
2458833.676260	20.9	2.0	HARPS

Note.–M-A Tel3, M-A Tel4, and M-A Tel6 are MINERVA-Australis Telescope3, Telescope4, and Telescope5, respectively.

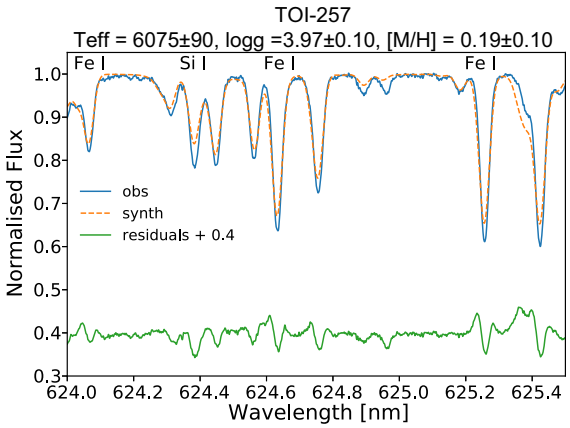

Figure 5. The best-fitting synthetic model spectrum from ISPEC (the red dashed line) of TOI-257 to that of the combined stellar spectrum obtained from the MINERVA-Australis spectroscopic observations (the blue solid line) for the wavelength region between 624.0 and 625.5 nm. The residuals of the fit are shown as the green solid line.

2.3.3 High-resolution spectroscopy with the high accuracy radial velocity planet searcher

We monitored TOI-257 with the high accuracy radial velocity planet searcher (HARPS) spectrograph ($R = 120\,000$, Mayor et al. 2003) on the ESO 3.6 m telescope at La Silla Observatory between December 2018 and November 2019. A total of 33 observations were obtained and the data was processed using the CERES pipeline (Brahm, Jordán & Espinoza 2017a). The exposure times were set to 300 s and taken using the high-precision radial velocity mode with simultaneous ThAr, providing a signal-to-noise ratio between 90 and 180 per resolution element at ∼510 nm. We produced radial velocities by cross-correlation with a G2-type binary mask template and derived the stellar properties as $T_{\rm eff} = 6178 \pm 80$ K, $\log g = 4.06 \pm 0.11$ dex, $[{\rm Fe/H}] = 0.32 \pm 0.05$ dex, and $v \sin i = 10.2 \pm 0.5\,{\rm km\,s^{-1}}$ for the host star with the HARPS spectra using ZASPE (Brahm et al. 2017b). The metallicity results from the HARPS spectra indicate that the star is definitively metal rich.

3 ANALYSIS

3.1 Host star properties from spectroscopy

We used the MINERVA-Australis spectra to determine TOI-257's atmospheric stellar parameters. Through the PYTHON package ISPEC (Blanco-Cuaresma et al. 2014; Blanco-Cuaresma 2019), we stacked the stellar spectra to derive the effective temperature, surface gravity, and overall metallicity ([M/H]) of the star. We configured the ISPEC synthetic grid to incorporate an MARCS atmospheric model (Gustafsson et al. 2008) and utilized the SPECTRUM (Gray & Corbally 1994) radiative transfer code. [M/H] was derived using version 5.0 of *Gaia*-ESO Survey's (GES) line-list (Heiter et al. 2015) normalized by solar values obtained by Asplund et al. (2009). Our synthetic spectra fit was constructed by setting initial values for $T_{\rm eff}$, $\log g$ and [M/H] of 6050 K, 4.44 dex, and 0.00 dex, respectively, based on the parameters from a broadband spectral energy distribution (SED) analysis with EXOFASTv2. Fig. 5 depicts our observed spectra and synthetic model produced by ISPEC. Our derived $T_{\rm eff}$, $\log g$ and [M/H] values were then fed into the Bayesian isochrone modeler ISOCHRONES (Morton 2015; Montet et al. 2015) that uses the Dartmouth Stellar Evolution Database (Dotter et al. 2008).

ISOCHRONES uses nested sampling scheme called MULTINEST (Feroz, Hobson & Bridges 2009) to determine the stellar mass, radius, and age, which was then used to derive the stellar density and luminosity of TOI-257. For this particular analysis, we used the stellar parameter results from ISPEC as well as the parallax value from *Gaia* DR2 with G, H, J, K, V, and W1 magnitudes[4] as priors in the global fit. The spectroscopic stellar ISPEC and ISOCHRONES values can be found in Table 1 and are in good agreement with the SED analysis performed using EXOFASTv2 and the asteroseismology. We then incorporated the $T_{\rm eff}$ and [M/H] values derived from the ISPEC analysis of the MINERVA-Australis spectra as priors in the final EXOFASTv2 global fit of the data in Section 3.4 and stellar luminosity of $L = 4.57 \pm 0.16\ L_{\odot}$ derived from SED fitting as a prior in the asteroseismology analysis in Section 3.2. We also note that stellar atmospheric parameters derived from the HARPS spectra are in general agreement with the ones derived with the MINERVA-Australis spectra, though the HARPS spectra suggest that the star is definitely metal rich ([Fe/H] $= 0.32 \pm 0.05$ dex) while the MINERVA-Australis spectra is compatible with solar metallicity to within 2σ ([M/H] $= 0.19 \pm 0.10$ dex). Given that the SED analysis is in better agreement with the derived stellar parameter from the MINERVA-Australis spectra and the strong degeneracies in the model atmospheres with parameters such as $T_{\rm eff}$, metallicity, and $\log g$ (e.g. see, Hinkel et al. 2016), we have chosen to use the stellar atmospheric parameters from MINERVA-Australis in the global analysis.

3.2 Asteroseismology

3.2.1 Global asteroseismic parameters

To perform asteroseismic analysis on TOI-257, we produced a custom light curve using the *TESS* Asteroseismic Science Operations Center (TASOC, Lund et al. 2017) photometry pipeline[5] (Handberg et al., in prep.), which is based on software originally developed to generate light curves for data collected by the K2 Mission (Lund et al. 2015). The TASOC pipeline implements a series of corrections to optimize light curves for an asteroseismic analysis (Handberg & Lund 2014), including the removal of instrumental artefacts and of the transit events using a combination of filters utilizing the estimated planetary period. The photometric performance of the TASOC light curve was comparable to the light curve produced by the SPOC pipeline.

Solar-like oscillations are broadly described by a frequency of maximum oscillation power ($\nu_{\rm max}$) and a large frequency separation ($\Delta\nu$), which approximately scale with $\log g$ and the mean stellar density, respectively (see, García & Ballot 2019). The power spectrum of the Sector 3 light curve of TOI-257 displays a power excess near $\sim 1200\ \mu$Hz (Fig. 6), consistent with the spectroscopic $\log g$ and the expected frequency range from the *TESS* asteroseismic target list (ATL, Schofield et al. 2019). An autocorrelation of the power spectrum reveals a peak at a frequency spacing consistent with the location of the excess power (e.g. Stello et al. 2009). Furthermore, the amplitude of the power excess (~ 9 ppm) is consistent with the expected value from observations by *Kepler* (Huber et al. 2011). The addition of the Sector 4 light curve reduced the significance of the asteroseismic detection due to the slightly elevated noise level, and was thus discarded for the remainder of our analysis.

[4]From experience, we find that ISOCHRONES delivers more reliable results when using just the G, H, J, K, V, and W1 magnitudes instead of all the available magnitudes given in the literature for a star.
[5]https://tasoc.dk/code/

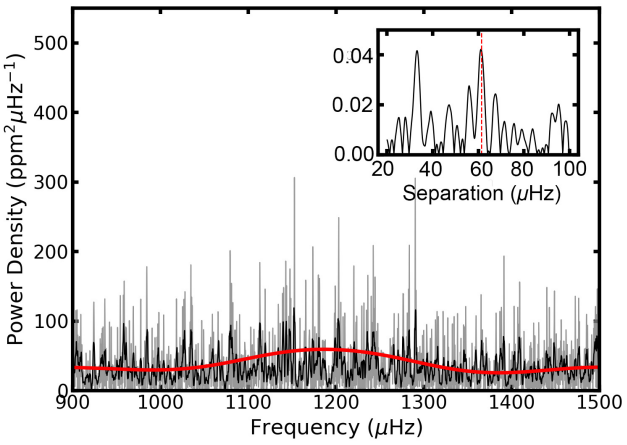

Figure 6. Power spectrum of the Sector 3 TASOC light curve of TOI-257 (grey line). The black and red lines show the power spectrum smoothed with a boxcar width of 2 μHz and Gaussian with a full width at half max of $\Delta\nu = 61.4$, respectively. The inset shows the autocorrelation of the power spectrum, with a red line marking the expected value of $\Delta\nu$ based on the location of the power excess.

To test the significance of the detection and measure $\nu_{\rm max}$ and $\Delta\nu$ we used 15 independent analysis methods within working group 1 of the *TESS* Asteroseismic Science Consortium (e.g. Huber et al. 2009; Mathur et al. 2010; Benomar et al. 2012; Kallinger et al. 2012; Mosser et al. 2012; Corsaro & De Ridder 2014; Davies & Miglio 2016; Campante 2018). All but one pipeline reported a significant detection of solar-like oscillations. The final parameters are $\nu_{\rm max} = 1188 \pm 40\ \mu$Hz and $\Delta\nu = 61.4 \pm 1.5\ \mu$Hz, with the central value taken from the solution closest to the median of all solutions, and uncertainties calculated from the median formal uncertainty returned by individual pipelines added in quadrature to the scatter over individual methods.

3.2.2 Grid-based modelling

We used a number of independent approaches to model the observed global asteroseismic parameters, including different stellar evolution codes (ASTEC, GARSTEC, MESA, and YREC, Christensen-Dalsgaard 2008; Weiss, Moffat & Kudelka 2008; Paxton et al. 2011, 2013, 2015; Choi et al. 2016a; Demarque et al. 2008) and modelling methods (BeSPP, BASTA, PARAM, isoclassify, Silva Aguirre et al. 2015; Serenelli et al. 2017; Rodrigues et al. 2014, 2017; Huber et al. 2017; García Saravia Ortiz de Montellano, Hekker & Themeßl 2018). Model inputs included the spectroscopic temperature and metallicity (see Section 3.1), $\nu_{\rm max}$, $\Delta\nu$, and the luminosity derived from the Gaia parallax and SED fitting. To investigate the effects of different input parameters, modelers were asked to provide solutions with and without taking into account the luminosity constraint.

The modelling results showed a bi-modality in mass (and thus age) at $\sim$1.2 and $\sim$1.4 $M_{\odot}$, with all pipelines favoring the higher mass solution once the luminosity constraint was included. We adopted the solution closest to the median of all returned values, with uncertainties calculated by adding the median uncertainty for a given stellar parameter in quadrature to the standard deviation of the parameter for all methods. This method has been commonly adopted for *Kepler* (e.g. Chaplin et al. 2014) and captures both random and systematic errors estimated from the spread among different methods. The final estimates of the stellar parameters,

Table 3. Asteroseismic stellar parameters for TOI-257.

Input parameters	
Frequency of maximum oscillation power, ν_{max} (μHz),	1188 ± 40
Large frequency separation, $\Delta\nu$ (μHz),	61.4 ± 1.5
Effective temperature, T_{eff} (K)	6075 ± 90
Metallicity, [Fe/H] (dex)	0.19 ± 0.10
Luminosity, L ($L_\odot$)	4.57 ± 0.16
Stellar Parameters	
Stellar mass, $M_\star$ ($M_\odot$)	1.390 ± 0.046 †
Stellar radius, $R_\star$ ($R_\odot$)	1.888 ± 0.033 †
Stellar density, $\rho_\star$ (cgs)	0.293 ± 0.011
Surface gravity, log g (cgs)	4.030 ± 0.011
Age, t (Gyr)	3.46 ± 0.43

Note. †Priors used in the EXOFASTv2 global fit.

taking into account the luminosity constraint, are summarized in Table 3, constraining the radius, mass, density, and age of TOI-257 to ∼2 per cent, ∼3 per cent, ∼3 per cent, and ∼13 per cent. We emphasize that these uncertainties in stellar parameters are robust against systematic errors from different stellar model grids, which are frequently neglected when characterizing exoplanets. The stellar mass and radius derived from this analysis is used as priors in the final EXOFASTv2 global fit of the data in Section 3.4.

3.3 Stellar rotation period estimates

The rotation period of TOI-257 was derived from the estimated stellar radius and by performing Lomb-Scargle (Scargle 1982) periodogram and auto-correlation function analysis (e.g. McQuillan, Aigrain & Mazeh 2013) on the *TESS* light curve, and measuring the projected stellar rotation velocity ($v \sin i$) from MINERVA-Australis spectra, assuming the axis of stellar rotation is perpendicular to the line of sight.

We calculated the Lomb-Scargle periodograms for the raw *TESS* light curves from Sectors 3 and 4 individually and from the combined light curve of the two sectors, after masking the transit events. For Sector 3, the periodogram shows that the variability has a period of $P = 5.01 \pm 0.46$ days and amplitude of $A = 114 \pm 2$ ppm. Sector 4 light curve has a variability with a period of $P = 4.13 \pm 0.22$ days and amplitude of $A = 144 \pm 2$ ppm. The period and amplitude from the two sectors is reasonably consistent. Performing this analysis on the combined light curves reveals that the variability has a period of $P = 4.04 \pm 0.13$ d, amplitude of $A = 88 \pm 1$ ppm, and false alarm probability (FAP)<<0.01. A second very strong peak is observed at ∼2.69 days (or 2P/3) in the Lomb-Scargle periodograms. The FAP was computed from Monte Carlo simulations (e.g. Messina et al. 2010) and the uncertainty in the period of variability was calculated following the procedure of Lamm et al. (2004). The variability from both sectors combined phases-up well at a period of 4.036 days as shown in Fig. 7, which indicates that the variability is likely to be astrophysical in nature (from stellar rotation and star spots) and not systematics. We therefore have adopted the period of variability as 4.04 ± 0.13 d.

We also performed an auto-correlation function analysis on the light curves from the individual sectors and combined sectors, and find that the period of variability as $P = 5.03 \pm 0.61$ days and $P = 4.12 \pm 0.32$ days for Sectors 3 and 4, respectively, and a period of $P = 4.14 \pm 0.22$ days for the combined light curves. We also find a strong secondary period in the combined light curves of ∼2.7 days. These results are consistent with the periods found from the Lomb-Scargle periodograms.

To determine whether the period of variability is the true rotation period of the star or one of its harmonics, we calculate an upper limit on the rotation period from the star's $v \sin i$ and estimated radius. We measured the $v \sin i$ of TOI-257 by fitting a rotationally broadened Gaussian (Gray 2005) to a least-squares deconvolution profile (Donati & Collier Cameron 1997) obtained from the sum of all the spectral orders from the combined highest S/N MINERVA-Australis spectra of TOI-257. The resulting $v \sin i$ is 11.3 ± 0.5 km s^{-1} and combined with the stellar radius from asteroseismology of $R_\star = 1.888 \pm 0.033$ $R_\odot$, sets the upper limit on the rotation period for the star of ∼8.5 days, assuming that the inclination of the stellar rotation axis is near 90 deg to the line of sight.

Given the above analyses, we attribute the 4.04 day period of variability observed in the combined *TESS* light curve to be half the true rotation period of 8.08 ± 0.26 days (which gives a $v_{rot} = 2*\pi*R_\star/P_{rot} = 11.8$ km s^{-1}, consistent with the value of $v \sin i$). The very strong secondary peak observed at ∼2.7 days in both the Lomb-Scargle periodograms and the auto-correlation function analysis provides further evidence in support of the 8.08 ± 0.26 days being the true rotation period since the secondary peak corresponds nicely with the P_{rot}/3 harmonic. It is common for the observed rotational modulation to be at one or more of the harmonics, in particular at

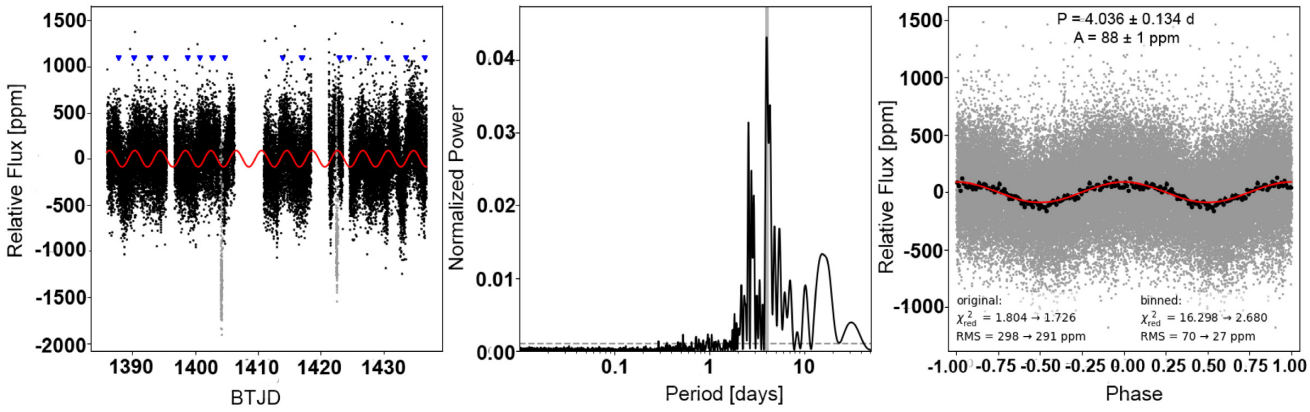

Figure 7. The left-hand panel shows the *TESS* light curve of TOI-257 from Sectors 3 and 4 with the best-fitting variability. The middle panel is the Lomb-Scargle periodogram for raw light curves from Sectors 3 and 4 combined. The right-hand panel is the phase-folded light curve at the peak period found from the Lomb-Scargle periodogram.

half and one-third the true rotation period (Vanderburg et al. 2016b). If the rotation period is 4.04 days, we would have expected to find a strong secondary peak at ∼2.02 days instead of ∼2.7 days. Given that the rotational period and stellar radius gives a rotational velocity consistent with the measured $v \sin i$, this suggests that the stellar obliquity is low (i.e. $i_\star \sim 90$ deg).

3.4 Planetary system parameters from global analysis

To determine the system parameters for TOI-257 and its planet, we used EXOFASTv2 (Eastman, Gaudi & Agol 2013; Eastman 2017; Eastman et al. 2019) to perform a joint analysis of the *TESS* photometry and the radial velocity data. We placed Gaussian priors on $T_{\rm eff}$ and [Fe/H] from the MINERVA-Australis high-resolution spectroscopy and Gaussian priors on $R_\star$ and $M_\star$ from asteroseismology. We applied an upper limit on the V-band extinction from the Finkbeiner (2011) dust maps at the location of TOI-257. We also performed a separate SED analysis (so as not to double count information used from the asteroseismic priors) as an independent check on the stellar parameters using catalog photometry from Tycho (Høg et al. 2000), 2MASS (Cutri et al. 2003), WISE (Cutri et al. 2013), and *Gaia* (Gaia Collaboration 2018b) as well as MIST stellar evolutionary models (Dotter 2016; Choi et al. 2016b). Gaussian priors were placed on the parallax from *Gaia* DR2, adding 82 μas to correct for the systematic offset found by Stassun & Torres (2018) and adding the 33 μas uncertainty in their offset in quadrature to the *Gaia*-reported uncertainty. For the quadratic stellar limb darkening coefficients u_1 and u_2, EXOFASTv2 applied weakly informative Gaussian priors drawn from the interpolation of the Claret & Bloemen (2011) limb darkening models at each step in $\log g$, $T_{\rm eff}$, and [Fe/H] taken in the global model to help guide the coefficients. Table 1 lists the broadband magnitudes used in the SED analysis and the stellar parameters including the ones used as priors in the global analysis.

We ran two global models with EXOFASTv2, an eccentric orbit model with $e\cos\omega_*$ and $e\sin\omega_*$ as free parameters and a circular orbit model with eccentricity fixed to 0 to determine the significance of any potential eccentricity. We computed the small-sample Akaike Information Criterion (AICc) and Bayesian Information Criterion (BIC, see, Akaike 1974; Burnham & Anderson 2002) for each model. We find that the Δ AICc between the eccentric and circular model is 4.03, indicating that the circular model is moderately preferred over the eccentric model. Therefore, we have chosen the one-planet circular model as the preferred solution. The results for analysis of both models are reported in Table 4.

The resulting best-fitting models for the transit light curves are plotted in Fig. 8, and for the radial velocities in Figs 9 and 10. Fig. 11 is a plot of the bisector velocity span showing no correlation between the bisectors and the radial velocities for the MINERVA-Australis observations, indicating that the measured radial velocity signal is likely planetary in nature and not due to stellar photospheric activity (Figueira et al. 2013).

From the best-fitting Kurucz stellar atmosphere model from the SED and the best-fitting MIST stellar evolutionary model, we find that TOI-257 is a somewhat evolved late-F star with $R_\star = 1.951^{+0.066}_{-0.051}\ R_\odot$, $M_\star = 1.35^{+0.12}_{-0.38}\ M_\odot$, $T_{\rm eff} = 6066^{+86}_{-110}$ K, and $\log g = 3.986^{+0.047}_{-0.150}$ (where g is in units of cm s^{-2}). These stellar parameters are in good agreement with the parameters derived from the MINERVA-Australis and HARPS spectroscopy and asteroseismology. However, we choose not to adopt these stellar parameters since they are not as precise as the ones derived from spectroscopy and asteroseismology and list the stellar parameters derived from the joint analysis of the *TESS* photometry and the radial velocity data in Table 4. From the joint analysis, we find that TOI-257 hosts a sub-Saturn sized planet with a radius of $R_P = 0.639 \pm 0.013$ R$_{\rm J}$ ($7.16 \pm 0.15\ R_\oplus$) and mass of $M_P = 0.138 \pm 0.023$ M$_{\rm J}$ ($43.9 \pm 7.3\ M_\oplus$), on a circular ∼18.4 day orbit.

To ensure that our results are not potentially biased from the use of the Claret & Bloemen (2011) limb darkening interpolation tables in EXOFASTv2, we ran two additional transit only circular models, one with and one without the Claret and Bloemen tables (setting the NOCLARET flag in EXOFASTv2 such that u_1 and u_2 are completely free parameters). Both transit only models provided consistent results confirming the stellar and planetary parameters are not being biased by the EXOFASTv2 Claret and Bloemen interpolation tables.

Whilst we do find that the circular model provides a somewhat better fit to the *TESS* light curve and radial velocity data than compared with the eccentric model, the planet could still be on an eccentric orbit given the $\sim 3.7\,\sigma$ eccentricity detection. As such, future transit observations to measure chromatic limb darkening as well as additional radial velocities can validate (or refute) any potential eccentricity in the orbit of TOI-257 b.

3.5 Complementary analysis, and limits on additional planets

We further analyse the radial velocity data set in Table 2 with RadVel (Fulton et al. 2018) to provide both an independent analysis for checking consistency in the mass and eccentricity of planet b, and to search for any additional planets. The search for additional planets is motivated by two reasons. First, moderately eccentric Keplerian signals can sometimes resolve into two near-circular resonant signals with additional radial velocity data (e.g. Wittenmyer et al. 2013; Trifonov et al. 2017; Boisvert, Nelson & Steffen 2018; Wittenmyer et al. 2019). Second, we wish to evaluate the multiplicity of systems like TOI-257 with warm sub-Saturns.

The combined analysis of the HARPS, MINERVA-Australis, and FEROS data sets are consistent with a planet at the known transiting period and T_c from Table 4. The circular orbital solution is marginally favored over an eccentric model (in agreement with the ExoFASTv2 analysis), according to the relative small-sample Akaike Information Criterion (ΔAICc = 3.14). We fix P and T_c to the values independently derived from the ExoFASTv2 analysis of the *TESS* light curve as they will not be well constrained from the RVs alone, considering the small baseline compared to the orbital period. The best-fitting semi-amplitude from RadVel is similar to the EXOFASTv2 result, 8.6 ± 1.2 m s^{-1}.

The remaining scatter in the residuals after removing planet b from the one-planet orbital solution is consistently larger than the measured uncertainties of the three instruments and appears structured (see Fig. 12). We use a custom-modified version of RadVel to generate log-likelihood periodograms (LLPs) with various orbit assumptions to search for additional planets. We start with a single planet model and generate a log-likelihood for a wide range in fixed periods, fitting only for T_c and K, as well as the relative instrument dependent offsets and additional radial velocity 'jitter' noise terms, and then a second LLP assuming a fixed period and T_c for planet b, but varying both semi-amplitudes to search for an additional planet candidate TOI-257c. Anecdotally, we observe that allowing for eccentric orbits in LLPs typically results in a noisier LLP compared to considering only circular orbits, and can particularly yield false peaks where $e \approx 1$ with the region of largest $|{\rm d}RV/{\rm d}t|$ located where the radial velocities are minimally sampled. These are likely non-physical orbits, so we only present circular searches (similarly, considering only eccentricities $\lesssim 0.5$ mitigates this effect).

Table 4. Median values and 68% confidence interval for TOI-257 from the MCMC EXOFASTv2 analysis of both eccentric and circular orbital models.

Parameter	Description	Eccentric model	Circular model			
Stellar parameters:						
M_*.....	Mass ($M_\odot$).....	1.394 ± 0.046	$1.407^{+0.045}_{-0.046}$			
R_*.....	Radius ($R_\odot$).....	1.883 ± 0.033	$1.867^{+0.033}_{-0.032}$			
L_*.....	Luminosity ($L_\odot$).....	$4.41^{+0.31}_{-0.29}$	$4.33^{+0.30}_{-0.28}$			
ρ_*.....	Density (cgs).....	$0.294^{+0.019}_{-0.017}$	$0.305^{+0.019}_{-0.018}$			
log g.....	Surface gravity (cgs).....	4.032 ± 0.021	4.044 ± 0.021			
$T_{\rm eff}$.....	Effective temperature (K).....	6096 ± 89	6095 ± 89			
[Fe/H].....	Metallicity (dex).....	0.177 ± 0.099	$0.175^{+0.099}_{-0.098}$			
Planetary Parameters:			b			
P.....	Period (days).....	18.38827 ± 0.00072	$18.38818^{+0.00085}_{-0.00084}$			
R_P.....	Radius ($R_{\rm J}$).....	$0.626^{+0.013}_{-0.012}$	0.639 ± 0.013			
M_P.....	Mass ($M_{\rm J}$).....	$0.134^{+0.023}_{-0.022}$	0.138 ± 0.023			
T_C.....	Time of conjunction ($\rm BJD_{TDB}$).....	2458385.7600 ± 0.0011 *	$2458385.7601^{+0.0013}_{-0.0012}$ *			
a.....	Semi-major axis (AU).....	0.1523 ± 0.0017	$0.1528^{+0.0016}_{-0.0017}$			
i.....	Inclination (degrees).....	$88.78^{+0.78}_{-0.57}$	$87.91^{+0.11}_{-0.10}$			
e.....	Eccentricity	$0.242^{+0.040}_{-0.065}$	0 (fixed)			
ω_*.....	Argument of Periastron (degrees).....	96 ± 22	...			
T_{eq}.....	Equilibrium temperature (K).....	1033^{+19}_{-18} ^	1027 ± 18			
$\tau_{\rm circ}$.....	Tidal circularization timescale (Gyr).....	1880^{+400}_{-360} ⋆	1750^{+380}_{-330} ⋆			
K.....	RV semi-amplitude ($\rm m\,s^{-1}$).....	8.5 ± 1.4	8.5 ± 1.4			
R_P/R_*.....	Radius of planet in stellar radii	$0.03414^{+0.00037}_{-0.00029}$	0.03521 ± 0.00022			
a/R_*.....	Semi-major axis in stellar radii	$17.39^{+0.36}_{-0.35}$	$17.60^{+0.36}_{-0.35}$			
δ.....	Transit depth (fraction).....	$0.001166^{+0.000025}_{-0.000020}$	0.001240 ± 0.000016			
τ.....	Ingress/egress transit duration (days).....	$0.00947^{+0.00160}_{-0.00072}$	$0.01532^{+0.00070}_{-0.00068}$			
T_{14}.....	Total transit duration (days).....	$0.2644^{+0.0017}_{-0.0013}$	0.2702 ± 0.0013			
b.....	Transit impact parameter	$0.28^{+0.17}_{-0.19}$	$0.643^{+0.019}_{-0.020}$			
ρ_P.....	Density (cgs).....	$0.67^{+0.13}_{-0.12}$	$0.65^{+0.12}_{-0.11}$			
$logg_P$.....	Surface gravity (cgs)	$2.927^{+0.072}_{-0.081}$	$2.922^{+0.070}_{-0.079}$			
Θ.....	Safronov number	$0.0467^{+0.0080}_{-0.0078}$	$0.0469^{+0.0078}_{-0.0076}$			
$\langle F \rangle$.....	Incident flux (10^9 erg $\rm s^{-1}$ $\rm cm^{-2}$).....	$0.245^{+0.018}_{-0.017}$	$0.253^{+0.019}_{-0.017}$			
T_P.....	Time of Periastron ($\rm BJD_{TDB}$).....	$2458367.59^{+0.68}_{-0.69}$	$2458385.7601^{+0.0013}_{-0.0012}$			
$e\cos\omega_*$.....	.....	$-0.026^{+0.083}_{-0.084}$	...			
$e\sin\omega_*$.....	.....	$0.225^{+0.040}_{-0.068}$	...			
M_P/M_*.....	Mass ratio	$0.000092^{+0.000016}_{-0.000015}$	$0.000094^{+0.000016}_{-0.000015}$			
d/R_*.....	Separation at mid transit	$13.42^{+1.20}_{-0.88}$	$17.60^{+0.36}_{-0.35}$			
Wavelength parameters:		*TESS* (Eccentric Model)	*TESS* (Circular Model)			
u_1.....	Linear limb-darkening coeff	0.222 ± 0.031	0.221 ± 0.032			
u_2.....	Quadratic limb-darkening coeff	0.274 ± 0.034	0.268 ± 0.033			
A_D.....	Dilution from neighboring stars	$\leq$0.00053	$\leq$0.00052			
Telescope parameters (eccentric model):		FEROS	HARPS	M-A T3	M-A T4	M-A T6
$\gamma_{\rm rel}$.....	Relative RV offset ($\rm m\,s^{-1}$).....	-5.6 ± 5.3	28.7 ± 1.5	1.0 ± 2.0	0.1 ± 2.0	-0.8 ± 2.1
σ_J.....	RV jitter ($\rm m\,s^{-1}$).....	$13.3^{+6.9}_{-4.3}$	$7.07^{+1.20}_{-0.94}$	$13.9^{+1.7}_{-1.4}$	$14.0^{+1.7}_{-1.4}$	$13.9^{+1.8}_{-1.5}$
σ_J^2.....	RV jitter variance	175^{+230}_{-95}	49^{+18}_{-12}	194^{+49}_{-37}	197^{+50}_{-38}	193^{+53}_{-40}
Telescope parameters (circular model):		FEROS	HARPS	M-A T3	M-A T4	M-A T6
$\gamma_{\rm rel}$.....	Relative RV offset ($\rm m\,s^{-1}$).....	-4.8 ± 5.3	29.3 ± 1.5	0.8 ± 2.0	-0.1 ± 2.0	-1.0 ± 2.1
σ_J.....	RV jitter ($\rm m\,s^{-1}$).....	$13.1^{+6.9}_{-4.2}$	$7.29^{+1.20}_{-0.98}$	$14.0^{+1.7}_{-1.4}$	$13.8^{+1.7}_{-1.4}$	$13.8^{+1.8}_{-1.5}$
σ_J^2.....	RV jitter variance	170^{+230}_{-92}	53^{+19}_{-13}	195^{+50}_{-38}	190^{+49}_{-37}	189^{+52}_{-40}

Table 4 – *continued*

Parameter	Description	Eccentric model	Circular model
Transit Parameters:		*TESS* LC1†	*TESS* LC2†
σ^2.....	Added variance	$1.70 \pm 0.12 \times 10^{-8}$	$1.33^{+0.60}_{-0.56} \times 10^{-8}$
F_0.....	Baseline flux	1.0000009 ± 0.0000034	1.000001 ± 0.000010
Model comparison statistics:		Eccentric model	Circular model
Δ AICc.....	Akaike information criterion	4.03	0
Δ BIC.....	Bayesian information criterion	17.34	0

Notes. – M-A T3, M-A T4, and M-A T6 are MINERVA-Australis Telescope3, Telescope4, and Telescope6, respectively.
*The time of conjunction that is closest to the starting value supplied as a prior and is typically a good approximation for the mid transit time.
^The equilibrium temperature of the planet assumes no albedo and perfect heat redistribution.
⋆The tidal circularization timescale is calculated using equation (3) from Adams & Laughlin (2006) and assuming a $Q = 10^6$.
†*TESS* LC1 is the *TESS* light curve from PDC and *TESS* LC2 is the *TESS* light curve produced using the Vanderburg et al. (2019) procedures.

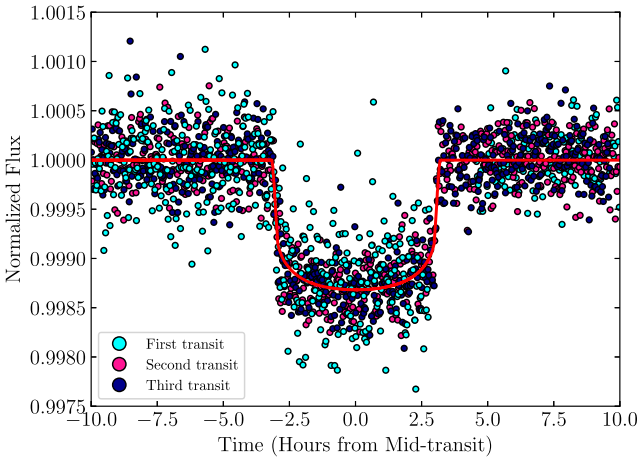

Figure 8. Phase-folded *TESS* light curve of TOI-257 with the individual transits colour coded similar to Fig. 2. The red solid line is the best-fitting model.

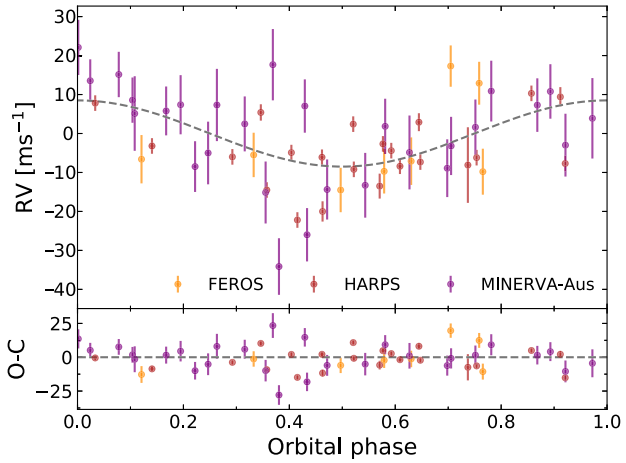

Figure 10. Same as Fig. 9 but phased to one orbital period. The units of the horizontal axis were chosen so that the transit mid-time corresponds to an orbital phase of 0.25.

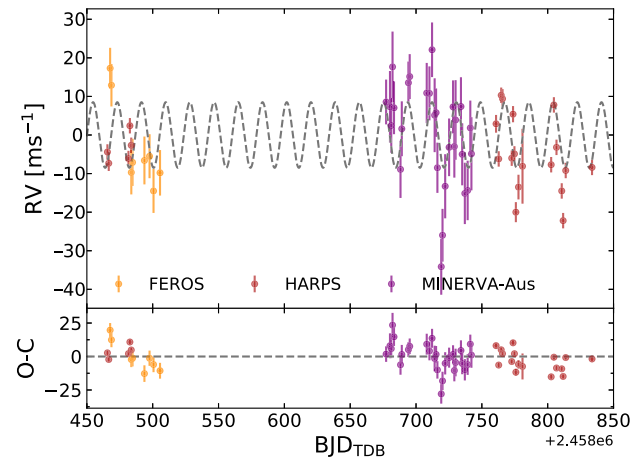

Figure 9. Radial velocity measurements of TOI-257 as a function of time. The radial velocity measurements from each instrument have been binned by day for clarity, however, the analysis was performed using the unbinned data. MINERVA-Australis radial velocities are represented by the purple filled-in circles. Radial velocities from FEROS and HARPS are the lime green and gold filled-in circles, respectively. The best-fitting model is plotted as the dashed grey line and the center-of-mass velocity has been subtracted. The bottom panel shows the residuals between the data and the best-fitting model.

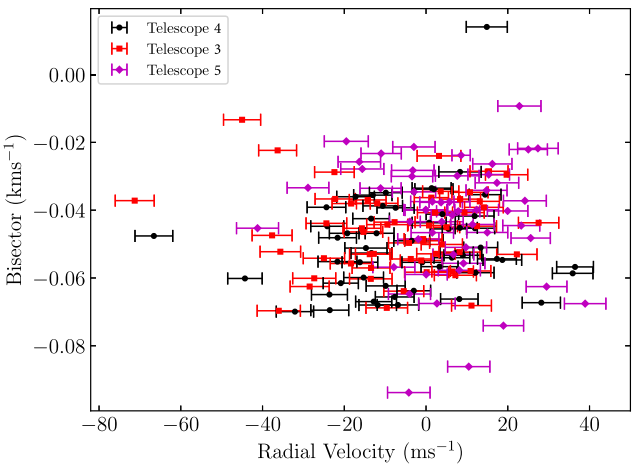

Figure 11. Bisector velocity span as a function of the radial velocities for the MINERVA-Australis radial velocities. There is no significant correlation between the bisector velocity span and the radial velocities.

Both the single-planet model LLP and the two-planet model LLP feature a peak near 71 days (Fig. 14). Including a circular planet near the 71-day peak, with no prior on T_c, yields a posterior probability distribution of the semi-amplitude for the second planet that is 7σ

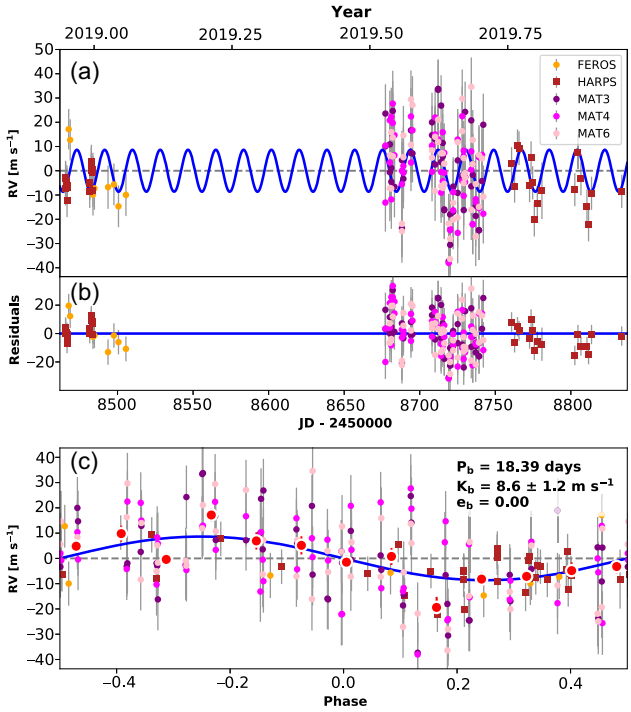

Figure 12. (a) Best-fitting one-planet Keplerian orbital model for TOI-257. The maximum likelihood model is plotted in blue. We add in quadrature the radial velocity jitter terms listed in Table 4 with the measurement uncertainties for all radial velocities to determine individual error bars. (b) Residuals to the best-fitting one-planet model. (c) Radial velocities phase-folded to the period of planet b. Red circles are the individual velocities binned in 0.08 units of orbital phase.

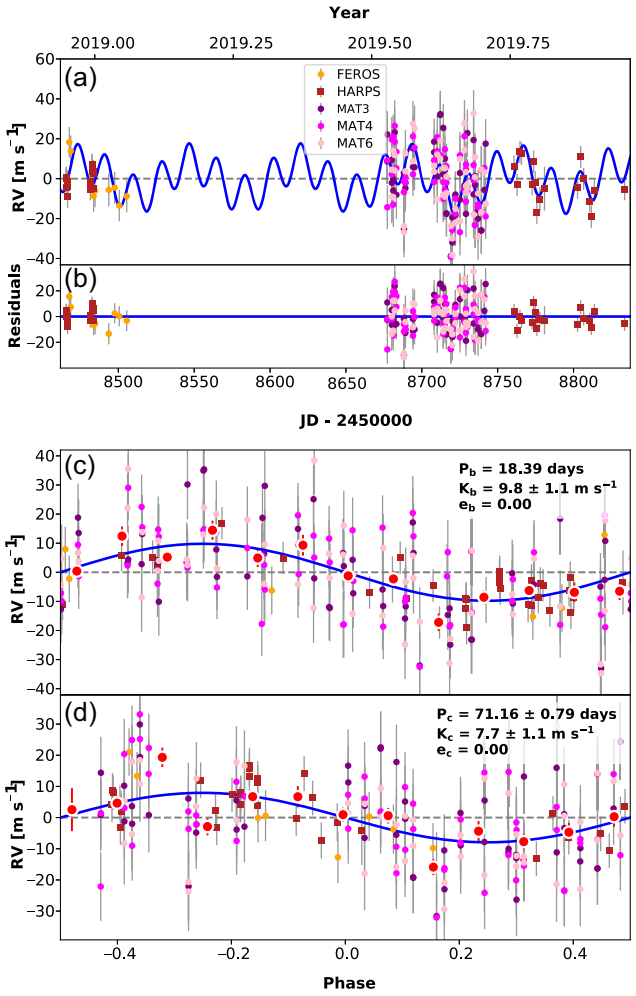

Figure 13. (a) Best-fitting two-planet Keplerian orbital model for TOI-257. The maximum likelihood model(s) is plotted in blue. We add in quadrature the radial velocity jitter terms listed in Table 4 with the measurement uncertainties for all radial velocities to determine individual error bars. (b) Residuals to the best-fitting 2-planet model. (c) Same, but radial velocities phase-folded to the period of planet b. (d) Same, but radial velocities phase-folded to the period of a possible planet c. Red circles (if present) are the individual velocities binned in 0.08 units of orbital phase.

deviant from 0, and minimally affects the statistical significance of the first planet (as shown in Fig. 13). The model comparison heavily favors the two-planet model over the one-planet model with ΔAICc = 38.10 (evidence ratio of 1.88×10^8). This 71-day signal translates to approximately a 0.2 per cent transit depth assuming the mass-radius relation given by Chen & Kipping (2017) and stellar parameters in Table 4. Posterior distributions plots from `RadVel` for a one-planet and two-planet circular models are available as supplementary material online.

As a consistency check with the two-planet preferred solution with `RadVel`, we ran an additional global model using `EXOFASTv2` that included fitting both planet b and c, with eccentricity fixed to 0 for both planets and using the same priors as before in our one-planet analysis. We used uniform priors on T_c and P for planet c, with the starting values on those parameters from the best-fitting TING values found with `RadVel`. We see no evidence for a transit in the *TESS* light curve within the uncertainty window of the best-fitting T_c for the possible outer planet with `RadVel` and have therefore excluded fitting transits for planet c in this analysis. The analysis with `EXOFASTv2` is unable to constrain the orbital parameters for planet c, resulting in a best-fitting period of $P = 378^{+98}_{-310}$ days and time of conjunction of $T_c = 2458709.7^{+20.0}_{-3.9}$ BJD. The best-fitting K is $9.8^{+7.6}_{-2.8}$ m s^{-1}. The orbital and planetary parameters for planet b remain consistent with the best-fitting values of the one-planet circular orbital model reported in Table 4. A comparison of the AICc and BIC between the two-planet and one-planet models gives a Δ AICc of 11.46 and Δ BIC of 46.23, strongly favouring the one-planet circular model. However, we note that the `EXOFASTv2` analysis was not able to reach full convergence in a reasonable amount of time and could be the source of discrepancy between `RadVel` and `EXOFASTv2`.

While this radial velocity detection is significant from the analysis with `RadVel`, more high-precision radial velocity measurements are needed to ensure the candidate c planet signal is not an alias or possibly a result of the observing cadence, especially without an observed transit event and the two-planet model being disfavored in the `EXOFASTv2` analysis.

3.6 Assessing the level of stellar activity present in the radial velocities

Next, we consider the possibility that the excess radial velocity residuals after modelling planet b are due to stellar activity rather than a second planet (or both) as presented in the previous subsection. At this time, `EXOFASTv2` does not permit the inclusion of a stellar activity model for the radial velocities, whereas `RadVel` does. With our customized version of `RadVel`, we calculate LLPs using a

Table 5. Gaussian and min/max priors for quasi-periodic hyper-parameters for TOI-257 used in `RadVel`.

Parameter	Unit; physical interpretation[a]	μ^b	σ	Min	Max	Citation
η_1	m s^{-1}, RV amplitude	10	None	0	100	stddev. of RVs, over-estimate
η_2	days, star-spot decay time-scale	10	5	0	100	Estimated from Giles, Collier Cameron & Haywood (2017), Fig. 5
η_3	Days, quasi-period	4.036 ($\times$ 2)	0.134 ($\times$ 2)	0	100	*TESS* light curve; Section 3.3, this paper
η_4	None, period length scale	0.3525	0.044	0	100	Dai et al. (2017), Haywood et al. (2018)

Note.–(a) These interpretations are further subject to the specific combination of values for the hyper-parameters, notably for cases with significantly different length and timescale factors. See Angus et al. (2018) for further discussion. (b) Also used for the initial guess.

Table 6. The relative Bayesian information criteria (Schwarz 1978) and small sample Akaike information criteria (AICc) (Akaike 1974) for the various models tested in `RadVel`. The GP model is marginally favored according to the AICc, but not the BIC. The candidate planet c is highly favored, however additional measurements will be necessary to confirm (or deny) its existence without a transiting event.

Model	Number of free parameters	Δ AICc	Δ BIC
b, c, GP, σ	18	0	8.80
b, c, σ	14	2.73	0
b, GP, σ	15	21.76	21.95
c, GP, σ	17	47.31	53.27
b, σ	11	40.44	28.78
c, σ	13	64.89	59.21
σ, GP	14	54.27	51.54
σ	10	81.10	66.41

Gaussian process (GP) with a quasi-periodic kernel (Rajpaul et al. 2015)[6] to approximate any detectable stellar activity. We re-run the MCMC analysis for one- and two-planet models. We assume broad Gaussian priors on the GP hyper-parameters listed in Table 5. Both ∼4- or ∼8-day GP period produce qualitatively similar LLPs and mitigate peaks less than the candidate $P_{\rm rot}$ and show strong evidence for both the transiting planet and the candidate planet near 71 days (Fig. 14). The GP model is strongly favored in the one-planet case, but only marginally so for the two-planet models (ΔAICc = 18.68, 2.73, respectively). However, a two-planet model with a GP is still favored over the corresponding one-planet model (ΔAICc = 21.76). A summary of the information criteria for the tested models is provided in Table 6. Posterior distribution plots from `RadVel` with a quasi-periodic Gaussian Process for a one-planet and two-planet circular models are available online as supplementary material.

Despite being statistically favored (∼5.1σ detection) with `RadVel`, we do not claim TOI-257c as a confirmed planet. Nava et al. (2019) has shown that activity can introduce spurious periodogram peaks at orbital periods longer than the stellar rotation period over the course of a single season, particularly for radial velocities that are unevenly sampled as is the case herein, notably for the HARPS data. However, with adequately sampled data (densely sampled with nightly cadence), Vanderburg et al. (2016b) find no evidence of spurious radial velocity periodogram peaks at periods longer than the stellar rotation period. As such, additional radial velocity monitoring over future seasons or novel stellar-activity mitigation approaches will be necessary to confirm or refute the candidate second planet signal at ∼71 days. Lastly, with no evidence for transits elsewhere in the light-curve, we can attribute the significant LLP peaks interior to planet b as a result of stellar-activity and/or a nightly observing cadence.

[6]The specific implementation of the quasi-periodic kernel in `RadVel` can be found on https://radvel.readthedocs.io/en/latest/tutorials/GaussianProcess-tutorial.html

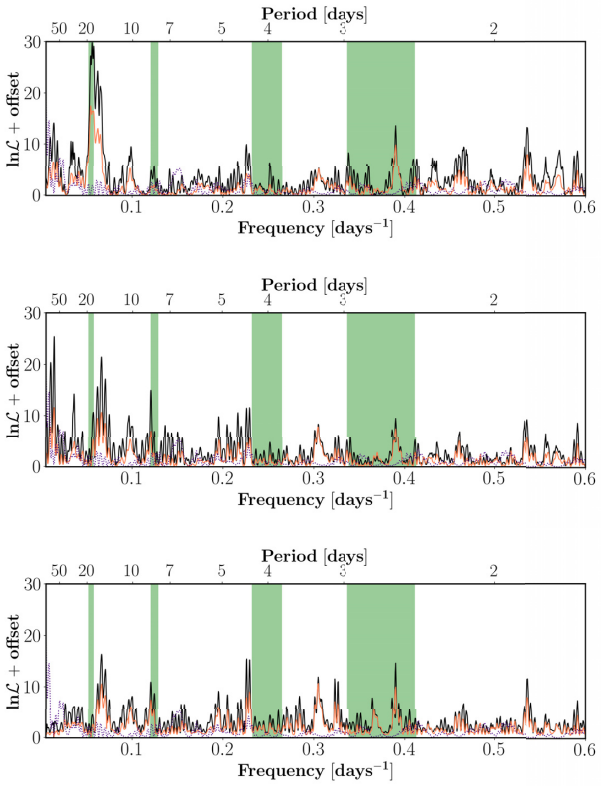

Figure 14. Log-likelihood periodograms as a function of frequency generated using `RadVel`. Shaded from left to right are the frequency of planet b (insignificant width), the estimated stellar rotation frequency $1/P_{\rm rot}$ from Table 5 (width is $\pm 1\sigma$), and harmonics $2/P_{\rm rot}$, $3/P_{\rm rot}$. The orange line includes a Gaussian process (GP) to model stellar activity with a quasi-periodic kernel with priors listed in Table 5, while the black line models remaining jitter as per-instrument Gaussian noise. The dashed line represents the window function (arbitrary scaling). Top: A one-planet circular model tested at a wide range in fixed periods, fitting for K, T_c and the relative instrument dependent offsets and noise terms (or single GP). Middle: Same, but for a two-planet model assuming a fixed period and T_c for planet b from Table 4, but varying both semi-amplitudes to search for additional planets. Bottom: Same as middle, but searching for a third planet such that $P_c \sim \mathcal{N}(71.5, 1)$. We see no evidence for additional periodic variations in the RVs past 18 days over the full observing window.

4 DISCUSSION

Here we have presented the discovery of TOI-257b, the first MINERVA-Australis led confirmation of a *TESS* transiting planet

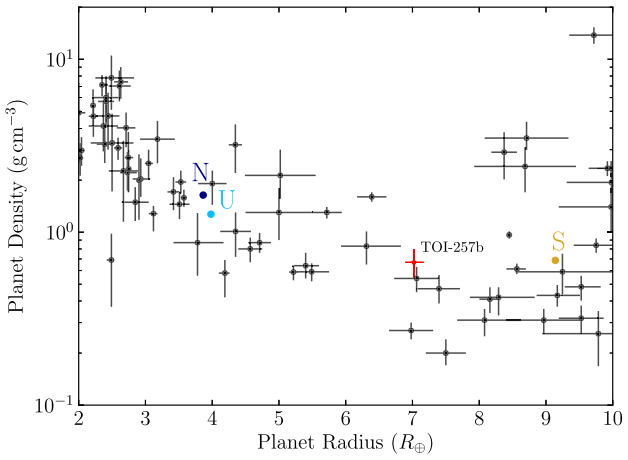

Figure 15. Planet radii versus density for Neptunian planets with R_P = 2−10 $R_\oplus$ and that have a density measured to better than 50 per cent. TOI-257b studied in this paper is labeled and plotted in red. The Solar System planets Saturn, Uranus, and Neptune are plotted as the gold-coloured letter S, light blue coloured letter U, and dark blue coloured letter N, respectively. Planets are taken from the NASA Exoplanet Archive (https://exoplanetarchive.ipac.caltech.edu/).

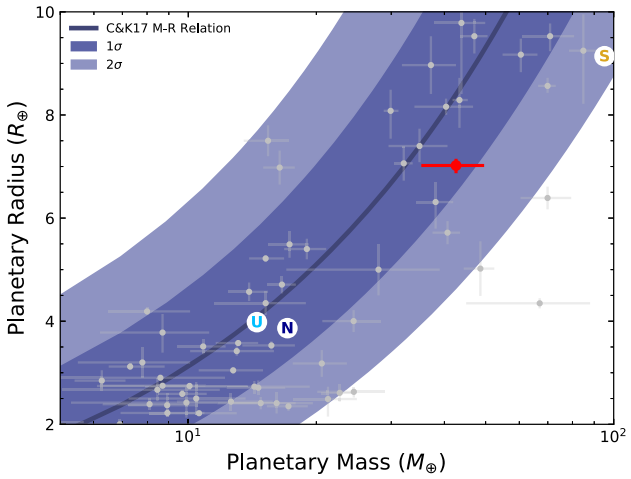

Figure 16. Planet mass versus radius for Neptunian planets with M_P = 5 − 100 $M_\oplus$ and R_P = 2−10 $R_\oplus$ measured to better than 50 per cent. The black line shows the Chen & Kipping 2017 probabilistic mass—radius relation for Neptunian worlds and the surrounding dark and light regions are the associated 68 per cent and 95 per cent confidence intervals, respectively. Similar to Fig. 15, TOI-257b is plotted in red and the Solar System planets Saturn, Uranus, and Neptune are plotted as the gold coloured letter S, light blue coloured letter U, and dark blue coloured letter N, respectively. Planets are taken from the NASA Exoplanet Archive (https://exoplanetarchive.ipac.caltech.edu/).

candidate. TOI-257b is a warm sub-Saturn planet with a radius ∼ 24 per cent smaller than Saturn (R_P = 7.16 ± 0.15 $R_\oplus$) and a mass ∼ 54 per cent less than Saturn (M_P = 43.9 ± 7.3 $M_\oplus$) on an orbit of $P = 18.38818^{+0.00085}_{-0.00084}$ days. The measured mass and radius give a mean density of $0.65^{+0.12}_{-0.11}$ g cm^{-3}, consistent with the density of Saturn (0.687 g cm^{-3}) and less dense than Jupiter (1.326 g cm^{-3}). Therefore, based on the mass, radius, and bulk density of this planet, it lies within the regime of planets classified as 'Neptunian worlds' by Chen & Kipping (2017). Further analysis of the radial velocity data also reveals hints for a second sub-Saturn mass planet (M_P = 70 ± 14 $M_\oplus$) in the system with an orbit of ∼71 days. However, additional high-precision radial velocity data is required to confirm the planet c candidate.

To understand the planet formation process, we must determine the bulk compositions of warm sub-Saturns such as TOI-257b, a class of planet which is absent from the Solar System. Such objects provide important data for astronomers studying planetary interiors because their masses are sufficiently small that their cores are not degenerate. That is, their mass and radius are dependent on each other such that the core and envelope mass fraction provides single family of solutions (e.g. Weiss & Marcy 2014; Petigura et al. 2016; Pepper et al. 2017; Petigura et al. 2017). For planets near the mass of Jupiter, cores are degenerate, and planetary radii are essentially independent of mass. Warm sub-Saturns represent an observational sweet spot where mass and radius are comparatively easy to measure, and when used to interpret the observations, standard models deliver a well-defined family of solutions for the planet's core/envelope mass ratio. This is particularly true for sub-Saturns with incident flux less than the ∼0.2 × 10^9 erg s^{-1} cm^{-2} limit where stellar irradiation can inflate planetary radii (Demory & Seager 2011). The incident flux for TOI-257b is ∼0.25 × 10^9 erg s^{-1} cm^{-2} and is very near this limit. Thus the effects of stellar irradiation on the radius of TOI-257b are likely negligible, allowing its internal structure to be modeled and highlights the significant value of discovering other similar planets with low incident flux.

Fig. 15 shows the radius-density diagram for Neptunian worlds (similarly defined after Chen & Kipping 2017 as those with radii from ∼2 to 10 $R_\oplus$). This classification also includes mini-Neptunes, sub-Saturns, and Saturns, planets that are dominated by large atmospheres of hydrogen and helium gas and are not significantly effected by gravitational self-compression. We show those planets for which the density has been measured to a precision of better than 50 per cent. TOI-257b has a mean density that is comparable to other exoplanets around the same size. Fig. 15 also shows the apparent trend of decreasing bulk density as a function of planet radius, indicative of the increasingly large volatile gas envelope up to around the radius of Saturn. Fig. 16 shows the mass-radius diagram for planets with masses between 5 and 100 $M_\oplus$ and radii between 2 and 10 $R_\oplus$ and for which they have been measured to a precision of better than 50 per cent with the Chen & Kipping 2017 probabilistic mass–radius relation for Neptunian worlds over-plotted. As evident in Fig. 16, TOI-257b lies within the 1σ uncertainty region of the mass–radius relationship as predicted by Chen & Kipping 2017.

The moderately low bulk density (0.65 g cm^{-3}) and relatively high equilibrium temperature (1027 K) for this planet as well as it orbiting a bright (J_{mag} = 6.504 ± 0.020 and K_{mag} = 6.256 ± 0.020) host star make it a potentially enticing target for follow-up atmospheric characterization from the upcoming James Webb Space Telescope (JWST). Using the transmission spectroscopy metric (TSM) of Kempton et al. (2018), we find that this planet has a TSM of ∼142. TSMs greater than 90 for Jovian and sub-Jovian planets are considered suitable for JWST transmission spectroscopy observations, making TOI-257 b an excellent target. However, this planet is not very suitable for emission spectroscopy given that the planet is on a relatively long period orbit and is cool compared to other planets with thermal emission measurements. We estimate that the expected secondary eclipse at 5 μm has a depth of ∼40 ppm (assuming blackbody emission), which would be challenging to measure, making this target less suitable for emission spectroscopy.

Measurements of the spin-orbit alignment for transiting warm Neptunian and Jovian worlds via the Rossiter-McLaughlin effect can provide powerful insights into the origins and migration histories of these planets (e.g. Queloz et al. 2000; Chatterjee et al. 2008; Winn et al. 2010; Naoz et al. 2011; Addison et al. 2018; Wang et al. 2018). Both classes of planets are strongly believed to have been formed beyond their hosts' protostellar ice line (for a dissenting view of the formation of close-in gas giant planets in-situ via the core-accretion process, see e.g. Batygin, Bodenheimer & Laughlin 2016; Hasegawa, Yu & Hansen 2019) and then experienced inward migration through one of two types of migration channels, quiescent migration through the disk (Lin, Bodenheimer & Richardson 1996) or chaotically dynamical high-eccentricity migration (Fabrycky & Tremaine 2007; Ford & Rasio 2008; Naoz et al. 2011). The latter migration mechanism is thought to be responsible for producing many of the known hot Jupiters due to the large observed range in their spin-orbit angles (e.g. see, Albrecht et al. 2012; Addison et al. 2013, 2018). However, it is unknown if this is the case for the warm sub-Saturn and Neptunian worlds like TOI-257b with orbits greater than 10 days. The limited sample of spin-orbit angles measured for these planet populations (only seven so far according to the TEPCat catalog,[7] see Southworth 2011) makes it difficult to draw any firm conclusions and more measurements are urgently needed. This planet presents a suitable candidate for studying the spin-orbit via the Rossiter-McLaughlin effect. We predict that the radial velocity semi-amplitude of the Rossiter-McLaughlin effect for TOI-257 to be $\sim$8 $\mathrm{m\,s^{-1}}$ based on the stellar and planetary parameters we obtained for this system. The predicted signal, while small, should be detectable on very high-precision ($\sim$1 $\mathrm{m\,s^{-1}}$) radial velocity facilities in the south such as on HARPS (Rupprecht et al. 2004), PFS (Crane, Shectman & Butler 2006), and ESPRESSO (Pepe et al. 2010). We predict, given the stellar rotational velocity (as determined from the rotational period and stellar radius) is consistent with the measured $v\sin i$ from spectroscopy (i.e. suggesting that the stellar obliquity is near 90 deg), that the projected spin-orbit angle λ when measured (whether aligned or misaligned) should be close to the true spin-orbit angle ψ.

5 CONCLUSIONS

We report the discovery of TOI-257b, a $R_P = 0.639 \pm 0.013\,\mathrm{R_J}$ ($R_P = 7.16\ R_\oplus$) and $M_P = 0.138 \pm 0.023\,\mathrm{M_J}$ ($M_P = 43.9\ M_\oplus$) transiting planet found by *TESS* and confirmed using radial velocity data from MINERVA-Australis, FEROS, and HARPS as well as direct imaging from SOAR and Zorro. We also find hints for an additional non-transiting long-period ($\sim$71 day) sub-Saturn mass planet candidate orbiting TOI-257 from analysis of the radial velocity data. TOI-257b belongs to a population of exoplanets between the sizes of Neptune and Saturn that appears to be rare. Furthermore, TOI-257b transits a very bright star ($V = 7.612$ mag) on a relatively long-period orbit of 18.423 days making it a great candidate for future follow-up observations to measure its spin-orbit alignment and transmission spectrum. Warm sub-Saturns such as TOI-257 b are important population of planets to study for understanding the formation, internal structures and compositions, and evolution and migration of giant planets. Future observational work of this planetary system will help to elucidate our understanding of these rare sub-Saturn planets that are absent in the Solar System.

[7] https://www.astro.keele.ac.uk/jkt/tepcat/

ACKNOWLEDGEMENTS

We thank the anonymous referee for their careful review of the manuscript that has led to significant improvements.

MINERVA-Australis is supported by Australian Research Council Linkage Infrastructure, Equipment and Facilities Grant LE160100001, Discovery Grant DP180100972, Mount Cuba Astronomical Foundation, and institutional partners University of Southern Queensland, University of New South Wales, Australia, Massachusetts Institute of Technology, Nanjing University, George Mason University, University of Louisville, University of California Riverside, University of Florida, and The University of Texas at Austin.

We respectfully acknowledge the traditional custodians of all lands throughout Australia, and recognize their continued cultural and spiritual connection to the land, waterways, cosmos, and community. We pay our deepest respects to all elders, ancestors, and descendants of the Giabal, Jarowair, and Kambuwal nations, upon whose lands the MINERVA-Australis facility at Mt Kent is situated.

Brendan P. Bowler acknowledges support from the National Science Foundation grant AST-1909209.

This research has made use of the NASA Exoplanet Archive, which is operated by the California Institute of Technology, under contract with the National Aeronautics and Space Administration under the Exoplanet Exploration Program. Funding for the *Transiting Exoplanet Survey Satellite (TESS)* mission is provided by NASA's Science Mission directorate. We acknowledge the use of public *TESS* Alert data from pipelines at the *TESS* Science Office and at the *TESS* Science Processing Operations Center. The results reported herein benefited from collaborations and/or information exchange within NASA's Nexus for Exoplanet System Science (NExSS) research coordination network sponsored by NASA's Science Mission Directorate. Based on observations obtained at the Gemini Observatory, which is operated by the Association of Universities for Research in Astronomy, Inc., under a cooperative agreement with the National Science Foundation (NSF) on behalf of the Gemini partnership: the National Science Foundation (United States), National Research Council (Canada), CONICYT (Chile), Ministerio de Ciencia, Tecnología e Innovación Productiva (Argentina), Ministério da Ciência, Tecnologia e Inovação (Brazil), and Korea Astronomy and Space Science Institute (Republic of Korea). Some of the Observations in the paper made use of the high-resolution imaging instrument Zorro at Gemini-South. Zorro was funded by the NASA Exoplanet Exploration Program and built at the NASA Ames Research Center by Steve B. Howell, Nic Scott, Elliott P. Horch, and Emmett Quigley. This research has made use of NASA's Astrophysics Data System.

Daniel Huber acknowledges support by the National Aeronautics and Space Administration through the *TESS* Guest Investigator Program (80NSSC18K1585) and by the National Science Foundation (AST-1717000). Ashley Chontos acknowledges support from the National Science Foundation through the Graduate Research Fellowship Program (DGE 1842402). William J. Chaplin, Warrick H. Ball, Martin B. Nielsen, and Andrea Miglio. acknowledge support from the Science and Technology Facilities Council and UK Space Agency. Funding for the Stellar Astrophysics Centre is provided by The Danish National Research Foundation (Grant DNRF106). Rafael Brahm acknowledges support from National Fund for Scientific and Technological Development Post-doctoral Fellowship Project 3180246, and from the Millennium Institute of Astrophysics (MAS). H.Z. Hui Zhang is supported by the Natural Science Foundation of China (NSFC grants 11673011, 11933001). Andres Jordan acknowledges support from FONDECYT project 1171208 and by the

Ministry for the Economy, Development, and Tourism's Programa Iniciativa Científica Milenio through grant IC 120009, awarded to the Millennium Institute of Astrophysics (MAS). Aldo M. Serenelli is partially supported by grants ESP2017-82674-R (Spanish Government) and 2017-SGR-1131 (Generalitat de Catalunya). Andrea Miglio acknowledges support from the European Research Council Consolidator Grant funding scheme (project ASTEROCHRONOMETRY, G.A. number 772293). Rafael A. Garcia acknowledges the support of the PLAnetary Transits and Oscillations of stars grant from the Centre National d'Études Spatiales. Savita Mathur acknowledges support from the Spanish Ministry with the Ramon y Cajal fellowship number RYC-2015-17697. Tiago L. Campante acknowledges support from the European Union's Horizon 2020 research and innovation programme under the Marie Skłodowska-Curie grant agreement No. 792848 (PULSATION). This work was supported by Foundation of Science and Technology/Ministry of Science, Technology and Higher Education through national funds (UID/FIS/04434/2019). Enrico Corsaro is funded by the European Union's Horizon 2020 research and innovation program under the Marie Sklodowska-Curie grant agreement No. 664931. L. González-Cuesta thanks the support from grant FPI-SO from the Spanish Ministry of Economy and Competitiveness (MINECO) (research project SEV-2015-0548-17-2 and predoctoral contract BES-2017-082610). Sarbani Basu acknowledges NASA grant NNX16AI09G and NSF grant AST-1514676. Ian J. M. Crossfield acknowledges support from the NSF through grant AST-1824644, and from NASA through Caltech/JPL grant RSA-1610091. Tansu Daylan acknowledges support from MIT's Kavli Institute as a Kavli postdoctoral fellow. Derek L. Buzasi acknowledges support from NASA through the TESS Guest Investigator program (80NSSC19K0385). Cenk Kayhan acknowledges support by Erciyes University Scientific Research Projects Coordination Unit under grant number MAP-2020-9749. Emilie Laychock and Michaela Collins acknowledge support by the National Science Foundation under grant 1559487. Victor Silva Aguirre acknowledges support from the Independent Research Fund Denmark (Research grant 7027-00096B) and the Carlsberg Foundation (grant agreement CF19-0649).

Resources supporting this work were provided by the NASA High-End Computing (HEC) Program through the NASA Advanced Supercomputing (NAS) Division at Ames Research Center for the production of the SPOC data products.

Software: Astropy (Astropy Collaboration et al. 2018), Matplotlib (Hunter 2007), DIAMONDS (Corsaro & De Ridder 2014), isoclassify (Huber et al. 2017), `EXOFASTv2` (Eastman et al. 2013; Eastman 2017; Eastman et al. 2019)

DATA AVAILABILITY STATEMENTS

The radial velocity data underlying this article are available in the article. The *TESS* photometric data is available at NASA's Mikulski Archive for Space Telescopes (https://archive.stsci.edu/). The raw direct imaging data and raw spectra will be shared on reasonable request to the corresponding author.

REFERENCES

Adams F. C., Laughlin G., 2006, ApJ, 649, 1004
Addison B. C., Tinney C. G., Wright D. J., Bayliss D., Zhou G., Hartman J. D., Bakos G. Á., Schmidt B., 2013, ApJ, 774, L9
Addison B. C., Wang S., Johnson M. C., Tinney C. G., Wright D. J., Bayliss D., 2018, AJ, 156, 197
Addison B. et al., 2019, PASP, 131, 115003
Akaike H., 1974, IEEE T.. Automat. Contr., 19, 716
Albrecht S. et al., 2012, ApJ, 757, 18
Anglada-Escudé G., Butler R. P., 2012, ApJS, 200, 15
Angus R., Morton T., Aigrain S., Foreman-Mackey D., Rajpaul V., 2018, MNRAS, 474, 2094
Asplund M., Grevesse N., Sauval A. J., Scott P., 2009, ARA&A, 47, 481
Astropy Collaboration, 2018, AJ, 156, 123
Barclay T., Pepper J., Quintana E. V., 2018, ApJS, 239, 2
Barnes S. I., Gibson S., Nield K., Cochrane D., 2012, Ground-based and Airborne Instrumentation for Astronomy IV, Vol. 8446. SPIE, p. 1053
Batygin K., Bodenheimer P. H., Laughlin G. P., 2016, ApJ, 829, 114
Bayliss D. et al., 2013, AJ, 146, 113
Benomar O., Baudin F., Chaplin W. J., Elsworth Y., Appourchaux T., 2012, MNRAS, 420, 2178
Blanco-Cuaresma S., 2019, MNRAS, 486, 2075
Blanco-Cuaresma S., Soubiran C., Heiter U., Jofré P., 2014, A&A, 569, A111
Boisvert J. H., Nelson B. E., Steffen J. H., 2018, MNRAS, 480, 2846
Brahm R., Jordán A., Espinoza N., 2017a, PASP, 129, 034002
Brahm R., Jordán A., Hartman J., Bakos G., 2017b, MNRAS, 467, 971
Brahm R. et al., 2016, AJ, 151, 89
Burnham K. P., Anderson D. R., 2002, Model Selection and Multimodel Inference. Springer-Verlag New York
Butler R. P., Marcy G. W., Williams E., Hauser H., Shirts P., 1997, ApJ, 474, L115
Campante T. L., 2018, in Campante T. L., Santos N. C., Monteiro M. J. P. F. G., eds, Asteroseismology and Exoplanets: Listening to the Stars and Searching for New Worlds, Vol. 49. Springer International Publishing, p. 55
Chaplin W. J., Elsworth Y., Davies G. R., Campante T. L., Handberg R., Miglio A., Basu S., 2014, MNRAS, 445, 946
Chatterjee S., Ford E. B., Matsumura S., Rasio F. A., 2008, ApJ, 686, 580
Chen J., Kipping D., 2017, ApJ, 834, 17
Choi J., Dotter A., Conroy C., Cantiello M., Paxton B., Johnson B. D., 2016a, ApJ, 823, 102
Choi J., Dotter A., Conroy C., Cantiello M., Paxton B., Johnson B. D., 2016b, ApJ, 823, 102
Christensen-Dalsgaard J., 2008, Ap&SS, 316, 13
Claret A., Bloemen S., 2011, A&A, 529, A75
Corsaro E., De Ridder J., 2014, A&A, 571, A71
Crane J. D., Shectman S. A., Butler R. P., 2006, in Proc. SPIE, Vol. 6269, p. 626931
Cutri R. M. et al., 2003, VizieR Online Data Catalog: 2MASS All-Sky Catalog of Point Sources (Cutri+ 2003), VizieR Online Data Catalog, p. II/246
Cutri R. M. et al., 2013, VizieR Online Data Catalog: AllWISE Data Release (Cutri+ 2013), VizieR Online Data Catalog, p. II/328
Dai F. et al., 2017, AJ, 154, 226
Davies G. R., Miglio A., 2016, Astronomische Nachrichten, 337, 774
Dawson R. I. et al., 2019, AJ, 158, 65
Demarque P., Guenther D. B., Li L. H., Mazumdar A., Straka C. W., 2008, Ap&SS, 316, 31
Demory B.-O., Seager S., 2011, ApJS, 197, 12
Donati J. F., Collier Cameron A., 1997, MNRAS, 291, 1
Dotter A., 2016, ApJS, 222, 8
Dotter A., Chaboyer B., Jevremović D., Kostov V., Baron E., Ferguson J. W., 2008, ApJS, 178, 89
Eastman J., 2017, EXOFASTv2: Generalized publication-quality exoplanet modeling code, Astrophysics Source Code Library, preprint (ascl:1710.003)
Eastman J., Gaudi B. S., Agol E., 2013, PASP, 125, 83
Eastman J. D. et al., 2019, preprint (arXiv:1907.09480)
Fabrycky D., Tremaine S., 2007, ApJ, 669, 1298
Feroz F., Hobson M. P., Bridges M., 2009, MNRAS, 398, 1601
Figueira P., Santos N. C., Pepe F., Lovis C., Nardetto N., 2013, A&A, 557, A93
Ford E. B., Rasio F. A., 2008, ApJ, 686, 621
Foreman-Mackey D., Morton T. D., Hogg D. W., Agol E., Schölkopf B., 2016, AJ, 152, 206
Fulton B. J., Petigura E. A., Blunt S., Sinukoff E., 2018, PASP, 130, 044504

Gaia Collaboration, 2018a, A&A, 616, A1
Gaia Collaboration, 2018b, A&A, 616, A1
García R. A., Ballot J., 2019, Living Rev. Solar Phys., 16, 4
García Saravia Ortiz de Montellano A., Hekker S., Themeßl N., 2018, MNRAS, 476, 1470
Giles H. A. C., Collier Cameron A., Haywood R. D., 2017, MNRAS, 472, 1618
Gray D. F., 2005, The Observation and Analysis of Stellar Photospheres, Cambridge University Press
Gray R. O., Corbally C. J., 1994, AJ, 107, 742
Gustafsson B., Edvardsson B., Eriksson K., Jørgensen U. G., Nordlund, Å., Plez B., 2008, A&A, 486, 951
Handberg R., Lund M. N., 2014, MNRAS, 445, 2698
Hasegawa Y., Yu T. Y. M., Hansen B. M. S., 2019, A&A, 629, L1
Haywood R. D. et al., 2018, AJ, 155, 203
Heiter U. et al., 2015, Phys. Scr, 90, 054010
Hinkel N. R. et al., 2016, ApJS, 226, 4
Howard A. W. et al., 2010, Science, 330, 653
Howard A. W. et al., 2012, ApJS, 201, 15
Howell S. B., Everett M. E., Sherry W., Horch E., Ciardi D. R., 2011, AJ, 142, 19
Huang C. X. et al., 2018, preprint (arXiv:1807.11129)
Huber D., Stello D., Bedding T. R., Chaplin W. J., Arentoft T., Quirion P.-O., Kjeldsen H., 2009, Commun. Asteroseismol., 160, 74
Huber D. et al., 2011, ApJ, 731, 94
Huber D. et al., 2017, ApJ, 844, 102
Hunter J. D., 2007, Comput. Sci. Engineer., 9, 90
Høg E. et al., 2000, A&A, 355, L27
Jenkins J. M. et al., 2016, in Proc. SPIE, Vol. 9913, p. 99133E
Kallinger T. et al., 2012, A&A, 541, A51
Kaufer A., Stahl O., Tubbesing S., Nørregaard P., Avila G., Francois P., Pasquini L., Pizzella A., 1999, The Messenger, 95, 8
Kempton E. M. R. et al., 2018, PASP, 130, 114401
Kinemuchi K., Barclay T., Fanelli M., Pepper J., Still M., Howell S. B., 2012, PASP, 124, 963
Kipping D., Nesvorný D., Hartman J., Torres G., Bakos G., Jansen T., Teachey A., 2019, MNRAS, 486, 4980
Lamm M. H., Bailer-Jones C. A. L., Mundt R., Herbst W., Scholz A., 2004, A&A, 417, 557
Lee E. J., Chiang E., Ferguson J. W., 2018, MNRAS, 476, 2199
Lin D. N. C., Bodenheimer P., Richardson D. C., 1996, Nature, 380, 606
Lissauer J. J., 1993, ARA&A, 31, 129
Lund M. N., Handberg R., Davies G. R., Chaplin W. J., Jones C. D., 2015, ApJ, 806, 30
Lund M. N., Handberg R., Kjeldsen H., Chaplin W. J., Christensen-Dalsgaard J., 2017, in European Physical Journal Web of Conferences, Vol. 160, p. 01005, preprint (arXiv:1610.02702)
Mathur S. et al., 2010, A&A, 511, A46
Mayor M., Queloz D., 1995, Nature, 378, 355
Mayor M. et al., 2003, The Messenger, 114, 20
McQuillan A., Aigrain S., Mazeh T., 2013, MNRAS, 432, 1203
Messina S., Desidera S., Turatto M., Lanzafame A. C., Guinan E. F., 2010, A&A, 520, A15
Montet B. T. et al., 2015, ApJ, 809, 25
Morton T. D., 2015, isochrones: Stellar model grid package. preprint (ascl:1503.010)
Mosser B. et al., 2012, A&A, 537, A30
Naoz S., Farr W. M., Lithwick Y., Rasio F. A., Teyssandier J., 2011, Nature, 473, 187
Nava C., Lopez-Morales M., Haywood R., Giles H., 2019, in AAS/Division for Extreme Solar Systems Abstracts, Vol. 51, p. 303.13
Nielsen L. D. et al., 2019, A&A, 623, A100
Paxton B., Bildsten L., Dotter A., Herwig F., Lesaffre P., Timmes F., 2011, ApJS, 192, 3
Paxton B. et al., 2013, ApJS, 208, 4
Paxton B. et al., 2015, ApJS, 220, 15
Pepe F. A. et al., 2010, in Ground-based and Airborne Instrumentation for Astronomy III, Vol. 7735, in Proc. SPIE, p. 77350F
Pepper J. et al., 2017, AJ, 153, 215
Petigura E. A. et al., 2016, ApJ, 818, 36
Petigura E. A. et al., 2017, AJ, 153, 142
Pollack J. B., Hubickyj O., Bodenheimer P., Lissauer J. J., Podolak M., Greenzweig Y., 1996, Icarus, 124, 62
Queloz D., Eggenberger A., Mayor M., Perrier C., Beuzit J. L., Naef D., Sivan J. P., Udry S., 2000, A&A, 359, L13
Quinn S. N. et al., 2019, AJ, 158, 177
Rafikov R. R., 2006, ApJ, 648, 666
Rajpaul V., Aigrain S., Osborne M. A., Reece S., Roberts S., 2015, MNRAS, 452, 2269
Ricker G. R. et al., 2015, J. Astronom. Telescop. Instrum. System., 1, 014003
Rodrigues T. S. et al., 2014, MNRAS, 445, 2758
Rodrigues T. S. et al., 2017, MNRAS, 467, 1433
Rupprecht G. et al., 2004, Ground-based Instrumentation for Astronomy, Vol. 5492, in Proc. SPIE, p. 148
Santerne A. et al., 2012, A&A, 545, A76
Santerne A. et al., 2016, A&A, 587, A64
Scargle J. D., 1982, ApJ, 263, 835
Schlafly E. F., Finkbeiner D. P., 2011, ApJ, 737, 103
Schofield M. et al., 2019, ApJS, 241, 12
Schwarz G., 1978, The Annals of Statistics, 6, 461
Serenelli A. et al., 2017, ApJS, 233, 23
Silva Aguirre V. et al., 2015, MNRAS, 452, 2127
Southworth J., 2011, MNRAS, 417, 2166
Stassun K. G., Torres G., 2018, ApJ, 862, 61
Stassun K. G. et al., 2019, AJ, 158, 138
Stello D. et al., 2009, ApJ, 700, 1589
Sullivan P. W. et al., 2015, ApJ, 809, 77
Tanigawa T., Ikoma M., 2007, ApJ, 667, 557
Tokovinin A., 2018, PASP, 130, 035002
Trifonov T. et al., 2017, A&A, 602, L8
Twicken J. D., Clarke B. D., Bryson S. T., Tenenbaum P., Wu H., Jenkins J. M., Girouard F., Klaus T. C., 2010, Software and Cyberinfrastructure for Astronomy, Vol. 7740, in Proc. SPIE, p. 774023
Vanderburg A., Plavchan P., Johnson J. A., Ciardi D. R., Swift J., Kane S. R., 2016b, MNRAS, 459, 3565
Vanderburg A. et al., 2016a, ApJS, 222, 14
Vanderburg A. et al., 2019, ApJ, 881, L19
Van Eylen V. et al., 2018, MNRAS, 478, 4866
Wang S., Addison B., Fischer D. A., Brewer J. M., Isaacson H., Howard A. W., Laughlin G., 2018, AJ, 155, 70
Wang S. et al., 2019, AJ, 157, 51
Weidenschilling S. J., 2005, Space Sci. Rev., 116, 53
Weiss L. M., Marcy G. W., 2014, ApJ, 783, L6
Weiss W. W., Moffat A. F. J., Kudelka O., 2008, Commun. Asteroseismol., 157, 271
Winn J. N., Fabrycky D., Albrecht S., Johnson J. A., 2010, ApJ, 718, L145
Wittenmyer R. A., Bergmann C., Horner J., Clark J., Kane S. R., 2019, MNRAS, 484, 4230
Wittenmyer R. A., Horner J., Carter B. D., Kane S. R., Plavchan P., Ciardi D., MINERVA-Australis consortium t., 2018, preprint (arXiv:1806.09282)
Wittenmyer R. A. et al., 2013, ApJS, 208, 2
Wittenmyer R. A. et al., 2020, MNRAS, 492, 377
Wright J. T., Marcy G. W., Howard A. W., Johnson J. A., Morton T. D., Fischer D. A., 2012, ApJ, 753, 160
Zhou G. et al., 2019, AJ, 158, 141
Ziegler C., Tokovinin A., Briceño C., Mang J., Law N., Mann A. W., 2020, AJ, 159, 19

SUPPORTING INFORMATION

Supplementary data are available at *MNRAS* online.

Figure S1. Posterior distributions from RadVel for all parameters for a 1-planet circular model.
Figure S2. Same as Fig. A1, but for a 2-planet circular model.

Figure S3. Posterior distributions for all parameters for a 1-planet circular model in RadVel with a quasi-periodic Gaussian Process to model stellar activity.
Figure S4. Same as Fig. A3, but for a 2-planet circular model.

Please note: Oxford University Press is not responsible for the content or functionality of any supporting materials supplied by the authors. Any queries (other than missing material) should be directed to the corresponding author for the article.

[1]*University of Southern Queensland, Centre for Astrophysics, West Street, Toowoomba, QLD 4350 Australia*
[2]*Sub-department of Astrophysics, Department of Physics, University of Oxford, Denys Wilkinson Building, Keble Road, Oxford, OX1 3RH, UK*
[3]*Department of Physics & Astronomy, George Mason University, 4400 University Drive MS 3F3, Fairfax, VA 22030, USA*
[4]*Department of Earth and Planetary Sciences, University of California, Riverside, CA 92521, USA*
[5]*Institute for Astronomy, University of Hawai'i, 2680 Woodlawn Drive, Honolulu, HI 96822, USA*
[6]*Department of Astronomy, University of Wisconsin-Madison, Madison, WI 53706, USA*
[7]*School of Physics and Astronomy, University of Birmingham, Birmingham B15 2TT, UK*
[8]*Stellar Astrophysics Centre (SAC), Department of Physics and Astronomy, Aarhus University, Ny Munkegade 120, DK-8000 Aarhus C, Denmark*
[9]*NSF Graduate Research Fellow*
[10]*Center for Astrophysics | Harvard & Smithsonian, 60 Garden Street, Cambridge, MA 02138, USA*
[11]*Dunlap Institute for Astronomy and Astrophysics, University of Toronto, 50 St. George Street, Toronto, Ontario M5S 3H4, Canada*
[12]*Facultad de Ingeniería y Ciencias, Universidad Adolfo Ibáñez, Av. Diagonal las Torres 2640, Peñalolén, Santiago, Chile*
[13]*Millennium Institute for Astrophysics, Faculty of Physics, Campus San Joaquin UC, Av. Vicuna Mackenna, 4860, Mascul, Santiago, Chile*
[14]*Space Telescope Science Institute, 3700 San Martin Drive, Baltimore, MD 21218, USA*
[15]*Astronomy Department, Indiana University Bloomington, 727 East 3rd Street, Swain West 318, IN 4740, USA*
[16]*Facultad de Ingeniera y Ciencias, Universidad Adolfo Ibáñez, Av. Diagonal las Torres 2640, Peñalolén, Santiago, Chile*
[17]*Department of Physics and Astronomy, University of Louisville, Louisville, KY 40292, USA*
[18]*Department of Physical Sciences, Kutztown University, Kutztown, PA 19530, USA*
[19]*Department of Physics & Astronomy, Vanderbilt University, 6301 Stevenson Center Ln., Nashville, TN 37235, USA*
[20]*Department of Physics, Fisk University, 1000 18th Ave. N., Nashville, TN 37208, USA*
[21]*Sydney Institute for Astronomy (SIfA), School of Physics, University of Sydney, 2006, Sydney, Australia*
[22]*Department of Astronomy, The University of Texas at Austin, Austin, TX 78712, USA*
[23]*Department of Physics and Astronomy, University of Kansas, 1251 Wescoe Hall Dr.,Lawrence, KS 66045, USA*
[24]*Department of Physics, Massachusetts Institute of Technology, Cambridge, MA 02139, USA*
[25]*Department of Astronomy, Yale University, New Haven, CT 06511, USA*
[26]*U.S. Naval Observatory, 3450 Massachusetts Avenue NW, Washington, D.C. 20392, USA*
[27]*Space Science & Astrobiology Division, NASA Ames Research Center, Moffett Field, CA 94035, USA*
[28]*Department of Physics and Astronomy, The University of North Carolina at Chapel Hill, Chapel Hill, NC 27599-3255, USA*
[29]*Instituto de Astrofísica, Pontificia Universidad Católica de Chile, Av. Vicuña Mackenna 4860, Macul, Santiago, Chile*
[30]*Department of Physics, Westminster College, 319 South Market Street, New Wilmington, PA 16172, USA*
[31]*MIT Kavli Institute for Astrophysics and Space Research, Massachusetts Institute of Technology, Cambridge, MA 02139, USA*
[32]*Exoplanetary Science at UNSW, School of Physics, UNSW Sydney, NSW 2052, Australia*
[33]*School of Astronomy and Space Science, Key Laboratory of Modern Astronomy and Astrophysics in Ministry of Education, Nanjing University, Nanjing 210046, Jiangsu, China*
[34]*Max-Planck-Institut für Astronomie, Königstuhl 17, Heidelberg 69117, Germany*
[35]*Earth and Planetary Sciences, Massachusetts Institute of Technology, 77 Massachusetts Avenue, Cambridge, MA 02139, USA*
[36]*Department of Astrophysical Sciences, Princeton University, 4 Ivy Lane, Princeton, NJ 08544, USA*
[37]*NASA Ames Research Center, Moffett Field, CA 94035, USA*
[38]*School of Physical Sciences, The Open University, Milton Keynes MK7 6AA, UK*
[39]*Department of Physics, Lehigh University, 16 Memorial Drive East, Bethlehem, PA 18015, USA*
[40]*Exoplanets and Stellar Astrophysics Laboratory, Mail Code 667, NASA Goddard Space Flight Center, Greenbelt, MD 20771, USA*
[41]*Perth Exoplanet Survey Telescope, Perth, Western Australia*
[42]*Center for Space Science, NYUAD Institute, New York University Abu Dhabi, PO Box 129188, Abu Dhabi, UAE*
[43]*Department of Chemistry & Physics, Florida Gulf Coast University, 10501 FGCU Blvd. S., Fort Myers, FL 33965 USA*
[44]*Instituto de Astrofísica e Ciências do Espaço, Universidade do Porto, CAUP, Rua das Estrelas, 4150-762 Porto, Portugal*
[45]*Departamento de Física e Astronomia, Faculdade de Ciências da Universidade do Porto, Rua do Campo Alegre, s/n, PT4169-007 Porto, Portugal*
[46]*INAF - Osservatorio Astrofisico di Catania, via S. Sofia 78, 95123, Catania, Italy*
[47]*Instituto de Astrofísica de Canarias (IAC), 38205 La Laguna, Tenerife, Spain*
[48]*Universidad de La Laguna (ULL), Departamento de Astrofísica, E-38206 La Laguna, Tenerife, Spain*
[49]*Universidade Federal do Rio Grande do Norte (UFRN), Departamento de Física, 59078-970, Natal, RN, Brazil*
[50]*IRFU, CEA, Université Paris-Saclay, F-91191 Gif-sur-Yvette, France*
[51]*AIM, CEA, CNRS, Université Paris-Saclay, Université Paris Diderot, Sorbonne Paris Cité, F-91191 Gif-sur-Yvette, France*
[52]*Center for Exoplanets and Habitable Worlds, Department of Astronomy & Astrophysics, 525 Davey Laboratory, The Pennsylvania State University, University Park, PA 16802, USA*
[53]*Max-Planck-Institut für Sonnensystemforschung, Justus-von-Liebig-Weg 3, 37077 Göttingen, Germany*
[54]*Institute of Astrophysics, University of Vienna, 1180 Vienna, Austria*
[55]*Department of Physics and Astronomy, Iowa State University, Ames, IA 50011 USA*
[56]*Department of Astronomy & Space Sciences, Erciyes University, Kayseri, Turkey*
[57]*LESIA, Observatoire de Paris, Université PSL, CNRS, Sorbonne Université, Université de Paris, 92195 Meudon, France*
[58]*Institute of Space Sciences (ICE, CSIC) Campus UAB, Carrer de Can Magrans, s/n, E-08193, Barcelona, Spain*
[59]*Institut d'Estudis Espacials de Catalunya (IEEC), C/Gran Capita, 2-4, E-08034, Barcelona, Spain*
[60]*Zentrum für Astronomy (ZAH/LSW) der Universität Heidelberg, Königstuhl 12, D-69117 Heidelberg, Germany*
[61]*HITS gGmbH, Schloss-Wolfsbrunnenweg 35, 69118 Heidelberg, Germany*
[62]*MIT Department of Physics, Massachusetts Institute of Technology, Cambridge, MA 02139, USA*

This paper has been typeset from a TEX/LATEX file prepared by the author.